MODELING AND CHARACTERIZATION OF MICROFABRICATED EMITTERS: IN PURSUIT OF IMPROVED ESI-MS PERFORMANCE

by

XINYUN WU

A thesis submitted to the Department of Chemistry

in conformity with the requirements for

the degree of Master of Science

Queen's University

Kingston, Ontario, Canada

December, 2011

Abstract

Electrospray ionization (ESI) has been an invaluable technique to mass spectrometry (MS) especially for analyzing large bio-molecules with unparalleled sensitivity, robustness, and simplicity. Great effort in the development of ESI technique has been devoted in the emitter design, as its shape and geometry have proved pivotal to the electrospray performance and further MS detection. Intrinsic problems for the traditional single-hole emitters including clogging and low throughput limit the applicability of the technique. To address this issue, the current project is focused on developing multiple electrospray (MES) emitters for improved ESI-MS analysis.

In this thesis, joint work of both computational fluid dynamic (CFD) simulations for electrospray and offline electrospray experiments for spray current measurement were performed. Numerical simulations were used to test the effect of various emitter designs on electrospray performance and the laboratory results serve as a guide and validation. The CFD code was based on Taylor-Melcher leaky dielectric model (LDM) and the transient electrospray process was successfully simulated. The method was first validated via a 750 μm inner diameter (i.d.) emitter and further applied to a 20 μm i.d. model. Different stages of the electrospray process were visually demonstrated and the quantitative investigations for the change of spray current under various applied electric fields and flow rates share good agreement with previous simulations and measurements. Based on the single-aperture prototype, MES simulations were performed with 2-hole and 3-hole emitters. Simulation predictions compared favorably with the experimental results. Evidence from this work has proved that CFD simulation can be used as an effective numerical tool to test emitter designs for MES. The benchmarking result on the successful simulation of a microscale emitter electrospray achieved in this work is believed to be the smallest scale of the dynamic simulation for electrospray published to date.

Co-Authorship

All research undertaken for this thesis was completed under the guidance of Dr. Natalie M. Cann and Dr. Richard D. Oleschuk. Part of the research work presented in Chapter 4 regarding multiple electrospray was co-authored by Ramin Wright, and the work was cited from the following paper in press:

Gibson,G.T.T.; Wright, R.D.; Oleschuk, R.D. *Multiple electrosprays generated from a single poly carbonate microstructured fibre.* Journal of Mass Spectrometry, 2011, in press.

Acknowledgements

I would like to thank my supervisors, Dr. Natalie M. Cann and Dr. Richard D. Oleschuk for their guidance, and inspiration throughout my graduate study and research. Lots of breakthroughs would not have been achieved without their insightful and constructive ideas. They have been the best advisors I could ever hope to have. Not only are they extraordinarily talented scientists, but more importantly, they are always caring for students and being there to help. I couldn't express how blessed I feel to be part of their research groups. As a relatively precedential project, I often felt I was struggling and inevitably, I had to confront lots of frustrating moments. Thanks so much for their encouragement all the way and the recognition for my work and ability, I was able to be where I am now.

I would like also to acknowledge my colleague Dr. Christopher Daub for always being so helpful and patient with my questions and generously providing me with lots of valuable ideas. Particular thanks to Dr. Graham Gibson for the critical guidance and help on my experimental work.

To my parents, for always being so supportive and believing in my potential and ability. It is out of their love that I would step so firmly forward whatever situation I am in. They are the origin of my endless enthusiasm and motivation.

Table of Contents

List of Figures

List of Tables

List of Abbreviations

2D	Two-Dimensional
3D	Three-Dimensional
AF	Area Fraction
BEM	Boundary Element Method
CE	Capillary Electrophoresis
CFD	Computational Fluid Dynamic
CNF	Carbon Nanofibers
CRM	Charged Residue Model
DEM	Dielectric Model
EHD	Electrohydrodynamics
ESI	Electrospray Ionization
FAVOR	Fractional Area Volume Obstacle Representation
FEM	Finite Element Method
HPLC	High Performance Liquid Chromatography
i.d.	Inner Diameter
IEM	Ion Evaporation Model

LC	Liquid Chromatography
LDM	Leaky Dielectric Model
MES	Multiple Electrospray
MS	Mass Spectrometry
MSFs	Micro-Structured Fiber
RSD	Relative Standard Deviation
VF	Volume Fraction
VOF	Volume of Fluid

Chapter 1 Introduction

The introduction of electrospray ionization (ESI) as a soft ionization method revolutionized the applicability of mass spectrometry (MS). The soft feature of the technique made possible the analysis of large bio-molecules like peptides and proteins directly from the liquid phase, due to its unique advantage of producing ions with a high relative number of charges [1]. The last decade has seen an incredible growth of ESI-MS and it is now extensively adopted in various biochemical disciplines including proteomics, metabolomics, glycomics, and as an identification tool for synthetic chemists [2-3]. ESI-MS is significantly more rapid, sensitive, and accurate than traditional techniques of mass determination for biological molecules such as gel electrophoresis. Moreover, the ability for large, non-volatile molecules to be analyzed directly from the liquid phase also enables its coupling to upstream separation techniques such as high performance liquid chromatography (HPLC) and capillary electrophoresis (CE) [4].

A typical ESI process generally includes droplet formation, droplet shrinkage and final formation of gas phase ions. Among the many factors that impact the performance of electrospray, the architecture of the emitter (i.e. geometry, shape, etc.) for spraying is a critical one. Traditional electrospray emitters are usually single-channel tapered or non-tapered ones fabricated by pulling or etching techniques. However, these emitters often suffer from problems like clogging, inadequate throughput etc. [5] There has been a clear evolution towards the development of novel emitter designs to generate multi-sprays for enhanced sensitivity and sample utilization.

The study of novel ESI emitter design has aroused great attention both experimentally and theoretically [3]. However, the difficulty in the direct comparison among studies becomes the hindrance since the complex physical process of ESI also relies on a lot of other variables besides tip geometry. Also, the cost for novel nano-emitter fabrication and testing can be considerably high. This thesis will address these problems by taking advantage of a CFD simulation tool to set up a virtual lab. It provides an ideally uniform physical condition for the comparison of various emitter designs without interconnected changes due to other parameters. Experimental measurements from a custom fabricated prototype will also be collected to provide both guidance and validation, to help form a better computational scheme. Particular emphasis will be placed on multi-nozzle emitter designs which we believe to be the main future platform in this field. Further fundamental studies of the factors that affect the electrospray behavior are also performed with respect to different geometric and operational parameters. This enables not only the development of more efficient and robust emitters, but may also enhance the application of ESI in broader areas.

1.1 Thesis Organization

This thesis starts with a discussion of fundamental aspects of the ESI technique. The following pages of this introduction present a brief literature review of the history of ESI and the theory behind the technique. Specifically, the evolution of different emitter designs and the basic theory of electrohydrodynamics (EHD) governing the ESI process will be discussed. In Chapter 2, the

experimental technique is described with emphasis on the setup for offline electrospray spray current measurement. Chapter 3 provides a description of the theoretical approaches employed in this study, the strategies and basis of our computational fluid dynamics (CFD) simulations. Chapters 4 and 5 present the experimental and theoretical results, respectively.

1.2 Fundamental Aspects of ESI

1.2.1 Brief History of ESI

The electrospray phenomenon, where a fine spray of charged droplets is generated in the presence of a strong electric field, has been known for almost one hundred years. It was not until the early 20th century that its significance to science was fully understood. A pioneering study of electrospray was carried out by physicist John Zeleny [6] in 1914 when he investigated the behavior of fluid droplets at the end of glass capillaries and the instability of electrified liquid surfaces. His report also presented experimental evidence for several electrospray operating regimes. Later, Malcolm Dole *et al.* [7] demonstrated the use of electrospray to ionize intact chemical species, which finally gave birth to the technique of ESI. In the 1980s, the technique was convincingly fine-tuned by John Fenn [8] and the discovery that high-mass bio-molecular ions could be extracted, intact, from ESI revolutionized MS. Up to that point, MS analysis had been limited to compounds or molecules which could be introduced as a vapor in a gas without decomposing in the ionization process. This ground-breaking contribution won John Fenn a share of the 2002 Nobel Prize for chemistry - the 4th time a Nobel Prize has been awarded to a mass

spectrometry pioneer. In their original papers, Fenn and his co-workers demonstrated the basic experimental principles and methodologies of the ESI technique as an ion source for MS, including soft ionization of involatile and thermally labile compounds, multiple charging of proteins, and intact ionization of complexes. Since then, ESI-MS has become an indispensible analytical tool in a number of scientific disciplines.

The strength of the ESI-MS technique is mainly its unparalleled ability to analyze large bio-molecules without fragmentation, its characteristic high sensitivity, high versatility, wide applicability, and the ability to couple directly to continuous flow methods like LC, CE *etc* [7]. Traditional ESI-MS has some limitations as well. These include the relatively low throughput, the control of the spraying mode, the sensitivity to the liquid physical properties and the electric field in the vicinity of the emitter tip etc. Research to improve ESI performance is an active scientific area.

1.2.2 Mechanism of ESI

The electrospray process is based on the application of a high voltage to a solution introduced through a capillary or an emitter with a small channel (Figure 1.1). Typically, the capillary is located 1-3 cm away from the counter-electrode (sampling orifice) which may be a plate with an orifice leading to mass spectrometric sampling system held at ground potential [9].

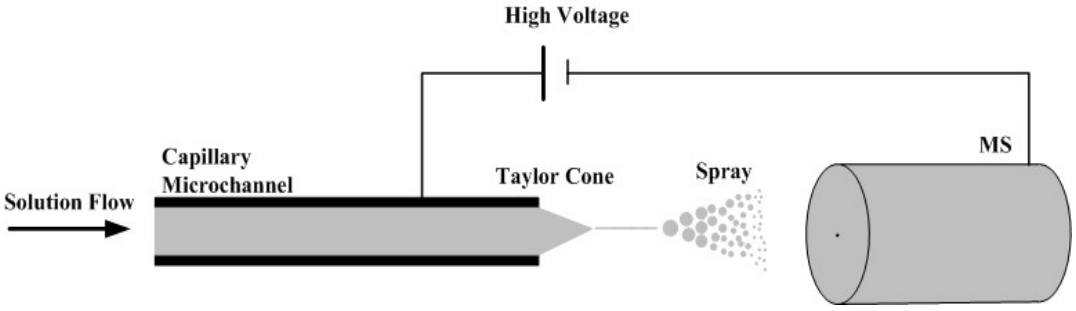

Figure 1.1 Schematic setup for ESI-MS technique

When a voltage is applied, the electric field will penetrate the solution. Positive ions present (if in positive ion mode) in solution will be electrically attracted towards the more negative potential and undergo electrophoretic movement to the counter electrode. As more and more excess charges accumulate at the surface, the liquid gradually deforms into a conical shape, referred to as a Taylor cone, in honor of G.I. Taylor [10] who described the phenomenon in 1964. As more excess charges accumulate at the interface, the charge density attains such a high value that the surface tension can no longer hold the emerging fluid together. A jet is then emitted from the apex of the Taylor cone [11]. The jet becomes unstable a short distance after and turns into a set of charged droplets. As the solvent evaporates, the size of the droplets is reduced while the charges within the droplet remain the same. When the electrostatic repulsion due to excess amount of like-charges at the surface of the droplet exceeds the surface tension, a process termed 'Coulomb fission' occurs. The process was first studied by Rayleigh who determined that it starts when $\boldsymbol{q}$, the total charge on the surface of the droplet whose radius is $\boldsymbol{R}$, reaches a 'Rayleigh stability limit', as defined by the Rayleigh equation below [12]:

$$q_R = 8\pi(e_0 \gamma R^3)^{1/2} \quad (1.1)$$

where e_0 is the permittivity of vacuum and γ is the surface tension. This equation gives the maximum charge a droplet with a certain radius can bear. Droplets will breakup into offspring droplets during the process because the Coulomb energy is lowered by spreading charges over a larger surface area [11].

A series of evaporation and Coulomb fission events occur until the resulting droplets are small enough to eventually produce gas-phase ions. The last step is especially relevant to MS detection, and the whole process of ESI is schematically illustrated in Figure 1.2.

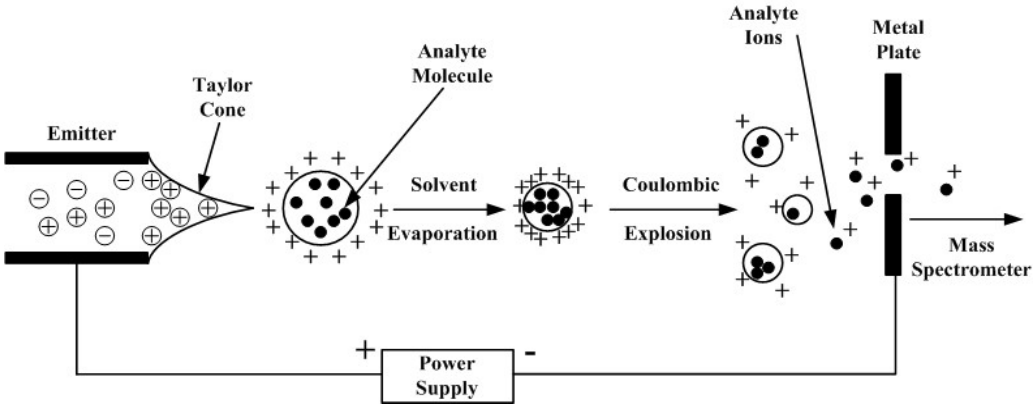

Figure 1.2 Schematic of major processes occurring in electrospray [5].

The key question in ESI-MS is the process by which gaseous ions are formed from the charged droplets. Concerning this process, two mainstream theories have been proposed. One is based on the charged residue model (CRM) suggested by Dole and co-workers in 1968 [7, 13]. CRM holds that when solvent evaporates, a sequence of Rayleigh instabilities (or Coulomb explosions), due to growing density of like charges, leads to droplet instability. Droplet

desolvation and Coulomb fission occur in turn and produce much smaller droplets which each contains only one solute molecule. That molecule then becomes a free gas phase ion by retaining some of the droplet's charge after the last of its evaporation steps. Studies suggest that this model is more favored in the gas-phase generation of large, globular proteins and non-covalent complexes. However, in most cases, this mechanism cannot explain the singly charged ionization process for low-mass ions [14-17].

The other assumption is based on the ion evaporation model (IEM) proposed by Iribarne and Thomson in 1976 [18]. It shares the same sequence of evaporation and Rayleigh instabilities with CRM but argues that, beyond a certain droplet size, gas-phase ions are emitted from the droplet rather than continuing the Coulomb fission. Despite having been studied for years, the actual mechanism by which desolvated gas-phase ions are produced is still under debate [19-28].

1.2.3 Operation of ESI

Since the capillary tip for spraying is very thin, the electric field around the capillary tip is very high. This value can be approximated as follows [11, 29-30]:

$$\boldsymbol{Ec = 2V_c/[r_c ln\left(\frac{4d}{r_c}\right)]} \tag{1.2}$$

where $\boldsymbol{V_c}$ is the applied potential, $\boldsymbol{r_c}$ is the outer radius of the capillary and $\boldsymbol{d}$ is the distance between capillary tip and the counter electrode. As shown in the Equation (1.2), the field $\boldsymbol{E_c}$ is proportional to the applied electric potential and inversely proportional to the radius of the emitter and the distance $\boldsymbol{d}$.

Smith [31] derived a rather useful equation for estimating the onset potential V_{on} (i.e. lowest potential required) for electrospray.

$$V_{on} \approx \left(\frac{r_c \gamma cos\theta}{2\varepsilon_0}\right)^{1/2} ln\left(\frac{4d}{r_c}\right) \tag{1.3}$$

where r_c is the radius of the capillary, γ is the surface tension of the liquid, θ is the half angle of the Taylor cone, ε_0 is the permittivity of vacuum. When replacing the parameter θ with 49.3° and ε_0 with constant 8.8×10^{-12} $J^{-1}C^2$, we have [32]

$$V_{on} = 2 \times 10^5 (\gamma r_c)^{1/2} \ln\left(\frac{4d}{r_c}\right) \tag{1.4}$$

The equation has been validated by many researchers in experiments [31, 33-34]. Generally in practice, in order to generate a stable electrospray, an electric potential of several hundred volts higher than the onset potential is required. Equation (1.4) provides a good reference for practitioners to choose a proper electric potential to start with when operating ESI. The equation also shows the importance of solvent choice for ESI. Table 1.1 [9] shows the calculated electrospray onset potentials for four solvents with different surface tensions for r_c= 0.1 mm and d = 40 mm. It indicates that it is generally much more difficult to operate Taylor cone-jet for solvent with a higher surface tension, e.g. water.

Table 1.1 Required onset voltages V_{on} calculated from Equation (1.4) for ESI of solvents with different surface tension γ [9]

Solvent	CH_3OH	CH_3CN	$(CH_3)_2SO$	H_2O
γ**(N/m)**	0.0226	0.030	0.043	0.073
V_{on}**(V)**	2200	2500	3000	4000

1.2.4 Operating Modes of ESI

The earliest observation from Zeleny's work [6] was that an electrospray may exhibit a wide variety of morphologies. By running the spray current through a telephone receiver and listening to the individual discharges, he identified dripping, pulsating, and cone-jet regimes. More elaborate classifications were further made from experimental observations, with burst [35] and astable [36] regimes identified.

Different spray modes ultimately determine the sensitivity and precision of MS detection. The cone-jet regime, discussed in Section1.2.2, has proven optimal in generating relatively large and stable spray current as well as smaller initial droplets that are prerequisites for higher sensitivity and quality MS analyses [37-39]. It was found that, depending on the analyte, the ion current can increase by a factor of 2-10 when it transitions from the pulsating to the cone-jet regime [37]. Ways to maintain a stable cone-jet mode throughout the experiment thus become desirable. A great step forward was achieved in 1994 by Fernandez de la Mora and Loscertales who found a simple scaling law for spray current versus flow rate in the case of highly conducting liquids [40]. Based on experimental values and dimensional analysis, they reported

$$\boldsymbol{I = f(\beta)\left(\frac{QK\gamma}{\beta}\right)^{1/2}} \tag{1.5}$$

where $\boldsymbol{I}$ and $\boldsymbol{Q}$ are the current and the flow rate, respectively and $\boldsymbol{\gamma}$, $\boldsymbol{K}$ and $\boldsymbol{\beta}$ are the liquid-gas surface tension, the electrical conductivity and the liquid to vacuum permittivity ratio respectively.

$f(\beta)$ is a dimensionless parameter to be determined experimentally. Equation (1.5) shows that the current emitted from a Taylor cone does not depend on the applied voltage and scales with the square root of the surface tension, conductivity, and flow rate of the liquid. In an effort to expand the parameter space, scaling laws have been derived that relate the spray current to the flow rate for more polar liquids [41]. These studies shed some light on how to actively control various parameters for ESI technique.

More recently, Smith *et al.* [38] presented a comprehensive study of parameters that affect the electrospray performance within the cone-jet regime. They clarified some of the factors crucial for maintaining the electrospray within the cone-jet regime including electric potential, flow rate, elution concentration and the distance between nozzle tip and MS orifice. Spray current was shown to be a reliable indicator for feedback of the ESI performance.

Despite the widespread adoption of ESI-MS, the lack of a detailed understanding of the mechanism sometimes impedes the rational choice of experimental parameters. Due to the complex physical mechanism and sensitive dynamics of the electrospray process, many users still tend to view the technique as a 'black box'. Sources of instability, interference, etc. are not always understood.

1.3 Development of Electrospray Emitters and State of the Art Research

While the emitter is a small component of the overall ESI process, it is the critical interface to couple the upstream sample manipulation system with a mass spectrometer. The growing interest

in emitters is mainly because its architecture impacts the size, shape, reproducibility and stability of the Taylor cone, thus determining the success of electrospray [3]. An ideal emitter would be able to attain low flow rates for highly sensitive detection, while at the same time allowing high flow rates for fast sample loading. It should also be robust enough to achieve high throughput for routine analysis [42-44]. These concerns are the key driving forces for the revolution in this field.

In Dole's first demonstration, a stainless steel hypodermic needle with an outer diameter of approximately 200 μm was used for the production of a 'molecular beam of macroions' [7]. However, the ionization efficiency generated by such a large-diameter emitter is poor due to the large size of the charged droplets that emanate from them. These droplets require a longer series of Coulomb explosions to form gaseous ions. With the growing need for better sensitivity (i.e. ionization efficiency), the clear movement is to miniaturize the aperture.

Nanoelectrospray, with flow rates less than 1,000 nL/min, started from the pioneering work of Wilm and Mann [45] in 1994 where they found a strong correlation between liquid flow rate and size of the emission zone from which droplets are ejected (see Equation (1.6)). And an illustration for the emission zone of the Taylor cone region is shown in Figure 1.3.

$$r_e = \left(\frac{\rho}{4\pi\gamma tan\left(\frac{\pi}{2}-\vartheta\right)\left[\left(\frac{U_\alpha}{U_\gamma}\right)^2 - 1\right]} \right)^{1/3} \times (dQ/dt)^{2/3} \qquad (1.6)$$

where $\boldsymbol{\rho}$ is the density of the liquid, $\boldsymbol{\gamma}$ is the surface tension of a liquid, □ is the liquid cone angle ($\vartheta = 49.3°$ for a classical Taylor cone model at equilibrium), U_α is the applied spray voltage, $\boldsymbol{U}$□ is the threshold voltage, and dQ/dt is the flow rate.

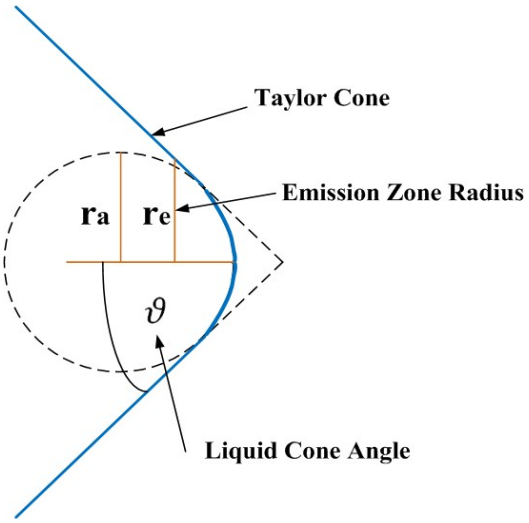

Figure 1.3 Illustration of detailed geometric parameters of a spraying Taylor cone where $\boldsymbol{r_a}$ is the radius of curvature of the best fitting circle at the tip of the cone; $\boldsymbol{r_e}$ is the radius of the emission region for droplets at the tip of a Taylor cone; $\boldsymbol{\vartheta}$ is the liquid cone angle.

Equation (1.6) indicates a smaller droplet is produced when the flow rate is lowered. It was demonstrated that, at nanoliters per minute flow rates, the droplets were small enough to yield gaseous ions without requiring as many fission events or as much desolvation from the ion source to the mass analyzer, providing distinctively higher sensitivity and improved sample utilization. These characteristics especially benefit the analysis of low abundance proteins, which are important to biomarker discovery for diseases and pharmaceutical research.

In order to attain stable electrospray signals at flow rates of nanoliters per minute, many tapered emitters have been fabricated using techniques such as pulling or chemically etching fused silica to create 1 to 20 μm sized apertures (Figure 1.4(A)). However, several critical problems have been encountered due to the nature of the small aperture of these single-tip tapered designs, including clogging and larger flow resistance which can seriously affect robustness (Figure 1.4(B)) [46]. To address these issues, etching methods have been developed to create a uniform i.d. while maintaining a tapered outside to stabilize the Taylor cone [47].

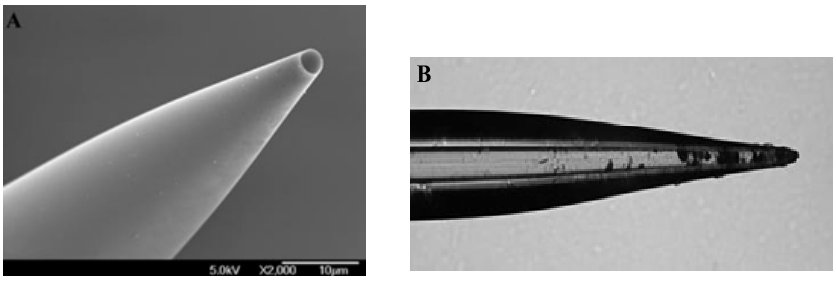

Figure 1.4 (A) Externally tapered emitter
(B) Optical image of a clogged tapered emitter with normal use [46].

Since, for most emitters, the base of the Taylor cone is defined by the outer diameter of the nozzle rather than the inner diameter of the hole, the issue of solvent wetting is significant. Many tip modifications, like hydrophobic coating with polymers [48-49], have been developed to make the surface less wettable.

In one approach, Liu *et al*. [50] presented an emitter designed using a perfluoroalkyl coating to restrict the base of Taylor cone to the large (75 μm) i.d. capillary exit. In their design, the Taylor cone was further stabilized by a nanotube carbon fiber protruding from the end of the

open capillary. The effectiveness of this novel design was further evaluated by Computational Fluid Dynamic (CFD) simulations for the ESI process [51]. From simulation results, a stable Taylor cone was clearly observed and it was confined to the sharp tip of the carbon fiber and the base of the Taylor cone was always limited to the inner periphery of the capillary.

A more recent trend in improving electrospray design [52-55] has been to integrate multiple emitters. Since the incoming flow is split in a multichannel emitter, the flow rate to each individual emitter is reduced. The intrinsic limitation on flow rates for single-hole emitters is avoided, and, at the same time, the lower flow rate increases the sensitivity and extends the lifespan of the emitter by reducing clogging. The improved sensitivity of multi-spray was first investigated by Tang *et al*. [52] and they found that the spray current was increased by a factor of the square root of the number of independent electrosprays relative to a single emitter at the same flow rate (Equation (1.7)), assuming that each emitter operates in cone-jet mode.

$$\boldsymbol{I_{total} = \sqrt{n} I_s} \tag{1.7}$$

where I total is the total multi-electrospray spray current, n the number of emitters, and I s is the spray current of an individual emitter. This equation is the deriving form of Equation (1.5).

In their work, a nine-emitter array was developed based on the multi-spray concept where the channels were arranged in a three-by-three configuration. This design showed a two-to-three times improvement in sensitivity at 1- 4 μL/min which agrees well with theoretical predictions. This also suggests that each emitter sprayed independently (Figure 1.5).

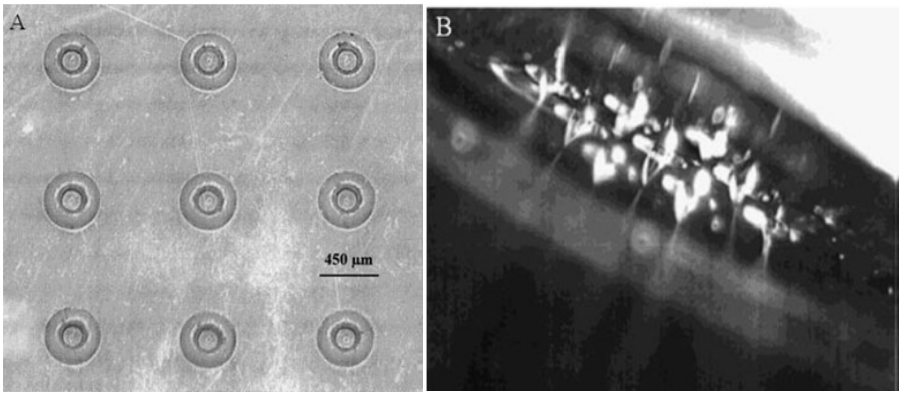

Figure 1.5 (A) Three by three configuration of an emitter array made with polycarbonate using laser ablation; (B) Photomicrograph of nine stable electrosprays generated from the nine-emitter array [52].

During the past few years, many novel designs of multiple electrospray emitters have been reported (for a good review, see [3].) In previous work in our lab [54], a series of robust and multichannel emitters have been designed. These are based on commercially available micro-structured fibers (MSFs), acting as a shower head to split the flow through its multiple channels

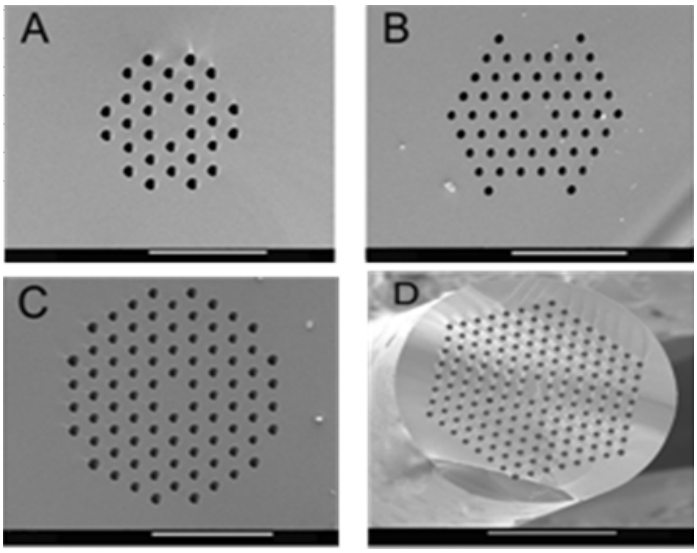

Figure 1.6 SEM images of the distal ends of four multichannel nanoelectrospray emitters and a tapered emitter: (A) 30 orifice emitter; (B) 54 orifice emitter; (C) 84 orifice emitter; (D) 168 orifice emitter; Scale bars in A, B, and C represent 50 µm, and 100 µm in D [54].

(Figure 1.6). The results showed improved resistance to clogging, more flexibility with flow rates, minimal backpressure, and more sensitivity, stability, and robustness.

However, for these emitters, the dense arrangement of holes led to significant cross-talk and the multi-sprays can coalesce (Figure 1.7). Therefore, the spray current gain was not as substantial as theoretically predicted. These results show the significance of the channel patterns (density *etc.*) in achieving true multi-spray and the importance of studying the factors that impact performance.

Deng *et al*. [53] indicated that, due to shielding, emitters at the periphery experience higher electric fields than the interior emitters for the same applied voltage and hence the emitters function in different regimes. The shielding can be caused by electrostatic interference between

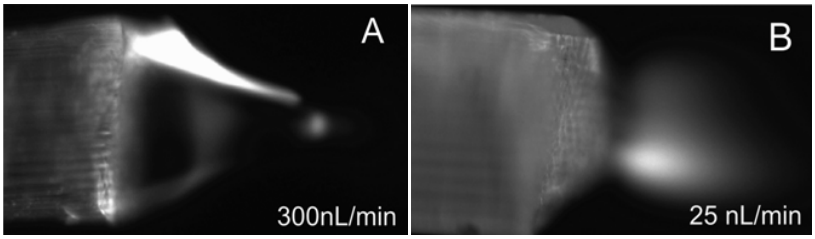

Figure 1.7 Photomicrographs of electrospray from of a 168-hole MCN emitter at different flow rates. (A) A traditional integrated Taylor cone observed from offline electrospray of water with 0.1% formic acid at 300 nL/min; (B) A mist of coalesced Taylor cones observed from offline electrospray at 25 nL/min[54].

neighboring emitters. This problem may ultimately limit the ability to develop multi-emitters because the severity of the shielding effect is proportional to the number of emitters. The arrangement of the holes within the emitter is critical. A circular arrangement of emitters was thus developed (Figure 1.8) and improved, to effectively minimize the non-uniformity of electric

fields experienced by the individual emitters in the array, enabling all the electrosprays to operate in the same regime.

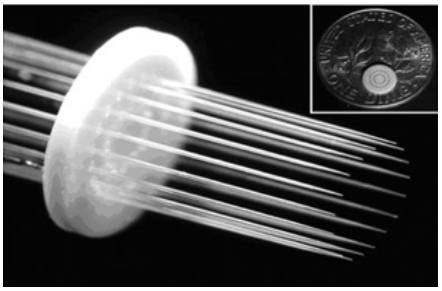

Figure 1.8 Circular arrays of etched emitters for better electric field homogeneity [53].

While multi-channel emitter fabrication is still a developing area, benefits like sensitivity gain, increased sample throughput, and improved clogging resistance have attracted great attention from areas including proteomics, metabolomics and glycomics, but also to the broader LC-MS community[3]. We believe future research in emitter design will largely involve the development of such platforms.

Currently, several problems greatly hinder research progress for emitter design:

A major one is the difficulty to make direct comparison of the emitter performance among different studies. Although spray or ion current (total or extracted) generated by the constant infusion of a sample has been widely adopted as a good standard, experiments on electrospray usually reveal reproducibility problems. During electrospray, too many factors besides the tip geometry greatly influence the spray behaviour and affect the measured current. Even though it is

always suggested that the whole set of parameters for operation be reported, the characterization results remain doubtful.

Another issue to consider is that experimental observation for the whole dynamic ESI process is extremely hard to achieve with currently available equipment. This makes cone-jet formation a 'black box' to practitioners and has also led to some disagreement and confusion in classifying various operational regimes in the past.

Also, the cost for nanoemitter fabrication and testing is high (e.g. the fiber used for our MSF design cost 27 000 Euro for 25 m). To supplant single tapered emitters as the industry standard, multi emitters and multichannel emitters will need to be more easily fabricated and cost competitive.

1.4 Theoretical Background of Taylor Cone-jet Formation

1.4.1 Basic Cone-jet Electrohydrodynamics (EHD)

Following the pioneering efforts made by Zeleny [6], who gave the first solid scientific description of the cone-jet mode, many physical models have been developed to better understand the EHD phenomenon of electrospray. However, due to the interdisciplinary nature of the field, which comprises aspects from electrostatics, electrokinetics, fluid dynamics etc., the literature on this subject is still very limited.

To simplify the complex physical situation, earlier studies mostly adopted either a perfect conductor model, or a pure insulating dielectric model with no free charges present at the liquid interface.

G.I. Taylor [35] took the initiative to describe the conical-shape cone formed in ESI based on a perfectly conducting liquid cone model. Taylor's derivation is based on two assumptions: the surface of the cone is an equipotential surface and the cone exists in steady state equilibrium. The solution to this problem is a hydrostatic equilibrium between the surface tension and the electrostatic stress normal to the gas-liquid interface. He showed that the equilibrium is obtained only when the half-angle at the apex of the cone is 49.3 degree, which is the celebrated Taylor cone angle. Taylor's model was a very important step in understanding the behavior of liquid cone-jets, and in fact corresponded well with many experimental results. Unfortunately, this model was unable to explain the formation of the thin jet which emerged from the cone apex, and the charged jet, in turn, modifies the potential distribution of the conical section and leads to deviations from Taylor's angle [56].

Glonti [57] and Nayyar and Murty [58] analyzed the Taylor cone-jet problem using the perfect dielectric model (DEM). According to DEM, fluids are assumed to be ideal insulators containing no free charge carriers and, hence, having zero electric conductivity. Under the influence of an electric field, polarized charges are formed at the interface between two media having different dielectric permittivity giving rise to a force that is always normal to the interface. The stationary deformation is determined using a balance of the normal stresses which occur due

to this force and due to interfacial tension. If polarization effects are homogeneous, electrical forces only appear at the fluid interface, where unbalanced dipoles are mechanically balanced by interfacial tension. Therefore, the liquid blows into a drop with surface always being elongated in the direction of the highest electric field (i.e. tip of the cone) into a prolate shape.

However, neither perfectly insulating fluids nor perfectly conducting fluids are found in the real world. Most applications deal with fluids of finite electrical conductivity. The problem becomes more interesting, yet more complicated, when finite conductivity of fluids is considered. Perhaps one of the most remarkable phenomena is the finding that, in addition to the prolate shape, a droplet in an electric field may be maintained in a spherical shape or even be deformed into an oblate spheroid as observed by Allan and Mason [59].

Realizing that perfect models are not good approximations for the physical phenomenon, Taylor further worked with J. R. Melcher [60] and together they established the Taylor-Melcher leaky dielectric model (LDM) which allows free charge carriers to exist in the dielectric fluid. Different from perfect conductors or dielectrics, in this case the interfacial charge is subjected to a tangential electric field and creates a tangential electric stress. It is this shear stress along the surface that ensures the formation of the cone-jet. In the case of LDM, viscous flow is developed to balance the force developed due to the tangential components of the field acting on the interfacial charge. A simple illustration of the physical model is provided in Figure 1.9.

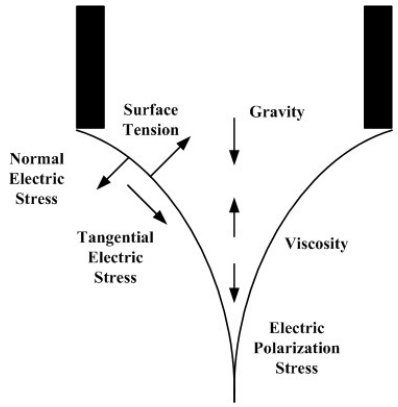

Figure 1.9 Distribution of forces in the liquid cone[51].

The establishment of the LDM formed an important step in the construction of a unified treatment of EHD. It also laid a solid foundation for researchers to access the electrospray mechanism and to understand various phenomena occurring in ESI experiments. Although the model has been improved and modified, the fundamental assumptions and concepts still remain unchanged. The LDM encompasses quite a wide range of phenomena in polar, as well as apolar, liquids.

Our simulations are based on the LDM. The related physical detail and governing equations will be discussed later. A good review paper on the LDM paper used for describing charged free jets has been published [61].

1.4.2 Numerical Modeling of Taylor Cone-jet Mode

Numerical modeling for electrospray is a challenging subject. The solution of the Navier–Stokes equations with a free surface or interface is not an easy task; this is complicated further when electrostatic effects are coupled to the fluid dynamics. From a physical perspective, the

complexity of the model stems from the non-trivial interaction between the evolving non-linear fluid jet structure, its electrical charges, and corresponding electric field [62]. This coupling manifests itself in the conical fluid structure from which the high speed jet explosively forms. During the transition step, the cone transforms into a jet at a reduction of the jet radius by an order of a hundred. This significant change makes it a tough mathematical and numerical problem. Thus most EHD problems have been addressed experimentally or with simplified theoretical models.

Hayati *et al.* first modeled the velocity field and calculated the electric field in a cone and in a jet with the finite element method (FEM) [56]. The shape of the liquid cone-jet was assumed at the onset of the simulation. Though the forces acting on the liquid cone were computed, the force field was not coupled to the momentum, and thus no deformation of the liquid was taken into account. Hartman [63-64] later presented a Lagrangian model of the coupled EHD equations. An initial cone shape was also assumed with a short jet ending in a semi-spherical shape. The model was able to calculate the shape of the cone-jet, the electric field within and outside the cone, and the surface charge density accumulated on the liquid surface. In a different approach, Yoon *et al.* presented a two-dimensional (2D), non-linear model by assuming a perfect conductor having all charges on the surface [65]. The boundary element method (BEM) was used to investigate oscillations of charged single and multi-jets. This is the first modeling work for multi-spays, although the governing equations were oversimplified.

Most of the work discussed above was based on an assumed initial shape of the liquid cone-jet and certain charge distribution. Also, they only describe the steady cone-jet mode. Recently, commercial codes such as ***FLUENT, FLOW-3D*** or ***CFX 4.4*** are becoming popular tools for scientific studies. These codes provide build-in physical models to solve the Navier–Stokes equations, and are flexible to be extended and adapted, for multidisciplinary applications (e.g. EHD problems). Zeng *et al.* [66], for the first time, reported a successful simulation of a transient, full-dimensional Taylor cone-jet by extending the function of a commercial CFD software, ***FLOW-3D***. Their model was based on the Melcher-Taylor leaky dielectric model using the Volume of Fluid (VOF) method. Similar simulations were later performed by Lastow *et al*. [67] using another commercially software package, CFX 4.4. They customerized the software by adding the additional electrical stress term for the momentum balance and Poisson's equation for the field distribution of electric potential. Recently, Liu *et al*. [55] employed the concept of multi-nanospray in a relatively large single capillary aperture (55 μm). They proposed an emitter model containing a multiple plumed array of carbon nanofibers (CNFs) vertically grown around the capillary orifice (Figure 1.10). CFD simulations were performed to test the feasibility of the design and investigate the performance of the CNF emitter with respect to several geometric and operational parameters. In the simulations, each CNF was shown to act as an individual electrospray emitter, resulting from the CNF tips. The simulations show that this novel emitter could generate a stable cone-jet for a wide range of flow rates, applied potential and liquid properties, thus making it suitable for MS analysis. Further study on the emitter geometry

suggested that the aspect ratio of the CNFs is the most important design factor affecting the spray performance. Though the functioning device has yet to be built and compared with simulations, the approach of taking advantage of CFD simulations proves to be a rather efficient way to test emitter design.

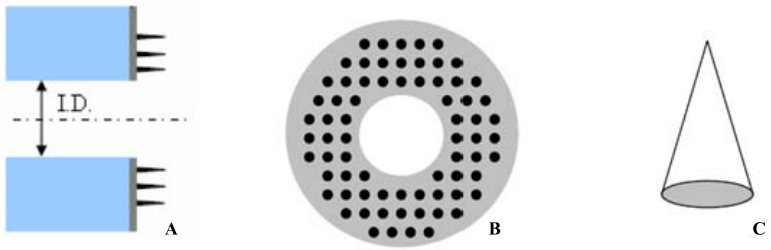

Figure 1.10 Schematic diagram of modeled open tubular emitter with array of CNFs around the capillary orifice: (A) vertical cross-section of the emitter model, (B) CNFs array around the orifice, (C) geometry of an individual CNF. [55]

1.5 Reseach Motivation and Approach

My project originated from the need to obtain a more complete and visualized picture of how the electrospray process performs with different emitter designs and under various operating conditions. The goal of this project is to create a flexible numerical tool to analyze factors that affect the electrospray process, such as surface charge density, the shape of the spray jet, ion current, jet size and velocity. The wealth of information obtained is expected to serve as a good reference to evaluate different designs for the microfabricated multi-nozzle electrospray emitters.

The project is both theoretical and experimental. Inspired by the successful modeling work done by Sen *et al*. [51, 55], we decided to perform CFD simulations on the complex EHD process

of electrospray using the ***FLOW-3D*** (Version 9.4, Flow Science Inc., Santa Fe, NM) [68]. CFD simulations will first be carried out to study the feasibility of this numerical tool in serving our purpose; then further simulation work will be performed on various models of realistic prototypes. Experimental results will be collected to serve as guidance and validation, and help form a better computational scheme.

Chapter 2 Characterization of Nanoelectrospray Emitters

In this chapter, the experimental setup and the experiments to characterize nanoelectrospray emitters will be discussed. The results are used as important guidance and validation for CFD simulation. Total ion current (TIC), or spray current, during the electrospray is measured via offline electrospray setup and serves as a good monitor of the spray performance. TIC measurement provides us with a simple picture of how electrospray performs since it measures ionization efficiency rather than the generation of charged droplets, where the dynamics are far more complex [3]. Also, a higher TIC implies a higher chance to get ionized and be sampled by MS, which we consider to be an important standard to compare among various emitter designs.

2.1 Solvent Choice

Since ESI performance relies on the nature of the analyte chosen, the same analyte is used for a direct comparison between studies. In this study, the spray solvent was composed of 50% water and 50% methanol containing 1% acetic acid (v/v). Glacial acetic acid, methanol (HPLC grade) were purchased from Fisher Scientific (Ottawa, ON, Canada) and used without purification. Deionized water was obtained from a Milli-Q filtration system (Bedford, MA, USA). The solvent has the following physical properties: density ρ = 1030 kg/m^3, viscosity = 0.008 Pa·s, surface tension coefficient = 0.037 N/m, dielectric constant = 55, electrical conductivity = 135×10^{-6} S/m.

2.2 Ion Source Assembly

In electrospray, a high potential difference is required. For typical non-conductive silicate emitters, making an efficient electrical contact with the solution that exits the tip is a challenge. Early attempts that have proved successful include: coating the emitter tip with a conductive material [43, 45, 69-70]; inserting a fine wire into the capillary tip to establish an electrochemical junction with the liquid [71-73]; and incorporating an electrode to make a liquid junction upstream of the emitter tip [74-77].

In our application, electrical contact with liquid was conveniently achieved via a micro-tee unit to create the liquid junction, as shown in the schematic drawing in Figure 2.1. The voltage is applied through the platinum wire in direct contact with the liquid within the junction. Two other unions (a sample introduction line on one side and an emitter on the other side) were connected horizontally through the other ports.

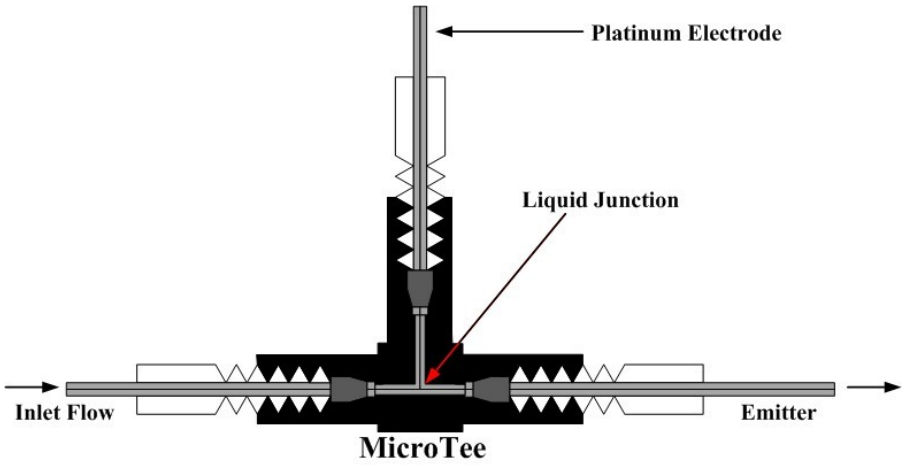

Figure 2.1 Schematic diagram of a MicroTee as a liquid junction

2.3 Preparation of Emitters

2.3.1 Commercial Single-nozzle Tapered Tip

The prototype TaperTip™ capillary strand (Figure 2.2) was ordered from New Objective (Woburn, MA, USA). It is designed for electrospray at a flow rate ranging from 0.2 to 3.0 µL/min and is specifically tailored at the tip to meet the rigorous demands of continuous-flow microspray and LC-MS. Each tip is video inspected to ensure that the shape and taper conform to design specification during manufacturing. The 50 cm capillary batch was further cut to 2 cm from the tip part with a thin ceramic plate piece to be used as an emitter.

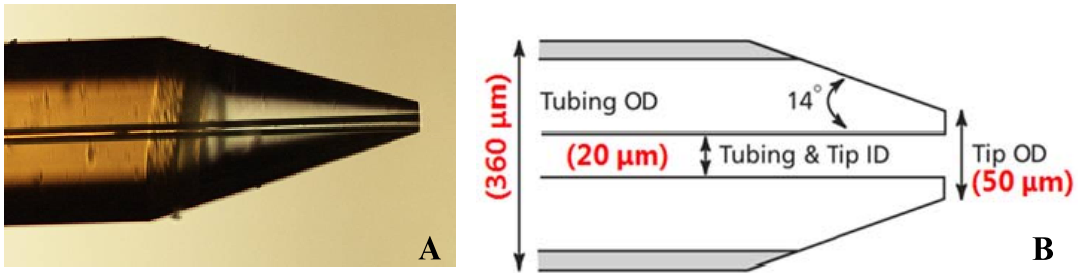

Figure 2.2 (A) Microscopic view for the single-channel emitter with external tapering at the tip; (B) The specifications of the emitter in (A).

2.3.2 Two-aperture Pulled Glass MSF

Glass MSF was ordered from Friedrich & Dimmock Inc. with two channels of diameter 25 µm, and a fiber diameter of 157 µm. The glass was further pulled under heat from a propane torch and gravity-assisted force. Two distinct spray channels can be seen with a diameter of about 5µm, and placed about 30 µm apart (see Figure 2.3).

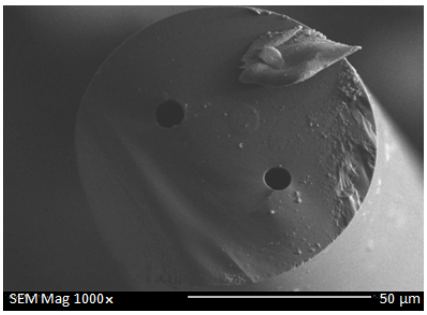

Figure 2.3 Scanning electron microscope image of the 2-channel pulled glass MSF.

2.3.3 Three-aperture Polycabonate MSF

A strand of 3-aperture MSF was first designed in our lab and further fabricated by Kiriama Pty Ltd company (Sydney, Australia) [78]. The 3-hole emitter is shown in Figure 2.4. The channels are arranged in a circular pattern to ensure every Taylor cone-jet experiences the same electric field. Each channel is 7 µm i.d., and all holes reside on a 435 µm circle leaving 100 µm from the fiber edge. The large distance between the holes is intended to generate independent MES.

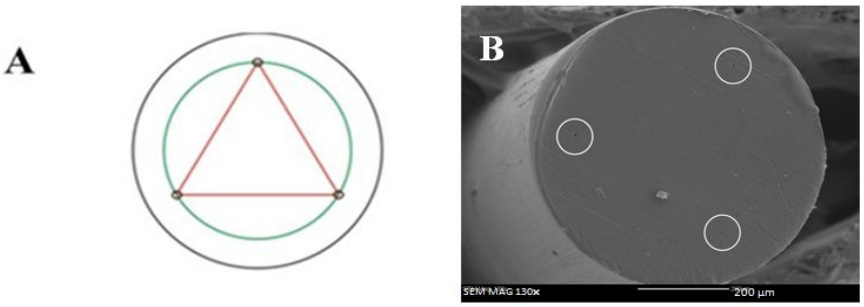

Figure 2.4 (A) Geometric specifications of the 3-hole design;
(B) Cleavage of the fabricated products according to our 3-hole emitter design showing the region of cutting and crack propagation.

2.4 Configuration of Offline Electrospray Test

The spray current measurement was carried out with a Keithley Picoammeter and a Tricep high voltage power supply (Figure 2.5) and the resulting Taylor cone-jet was further observed through a microscope (Nikon Eclipse Ti-S, Nikon Canada, Mississauga, ON, Canada) with a direct visualization system, Q-Imaging, Nikon microscope software (Compix Inc. Imaging Systems, 705 Thomson Park Drive, PA, USA) (see Figure 2.6).

The configuration of a typical offline electrospray test is illustrated in Figure 2.7. Aqueous electrospray samples (50% water and 50% methanol, containing 1% acetic acid) were delivered through the emitter which was set in a MicroTee^{TM} using a 0.5 mL Hamilton syringe driven by an 11 Plus pump (Harvard Apparatus, Holliston, MA, USA). Since the relative distance between the emitter tip and the MS orifice the position of an emitter is another influencing factor [79], a consistent distance was used in different runs to ensure a true comparison. To monitor the morphology of the Taylor cone-jet throughout the experiments as well as to accurately position the emitter, current electrospray apparatus was mounted directly on the optical stage. A positive high voltage supply was connected via a platinum wire electrode in contact with the mobile phase within the MicroTee. Voltage supply was provided by a TrisepTM-2100 high voltage module (Unimicro Technologies Inc. Pleasanton, CA, USA). The PicoammeterTM (Keithley Instruments Inc., Cleveland, OH, USA) linked to the counter electrode plate was used for spray current measurement where averaging signals were taken every 300 ms.

Figure 2.5 Workstation, picoammeter, and power supply respectively (from top to bottom).

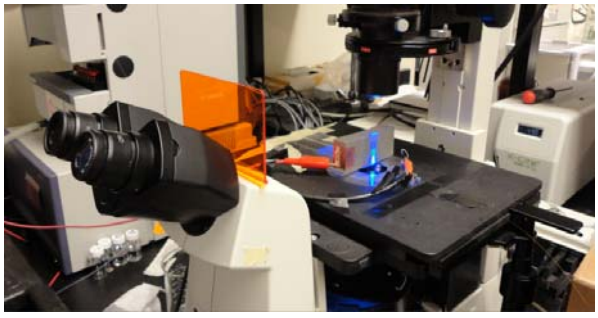

Figure 2.6 ESI apparatus for offline analysis with microscope imaging.

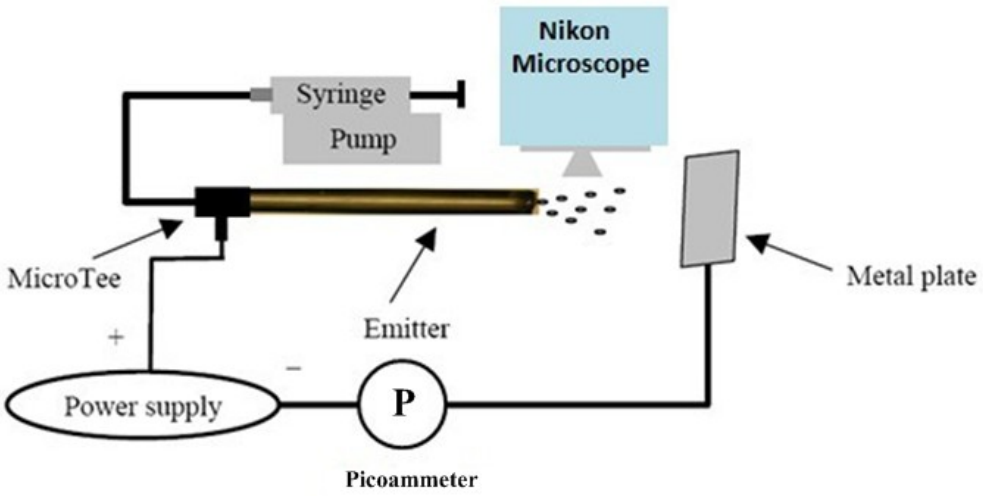

Figure 2.7 Schematic of an offline electrospray setup

Chapter 3 Theoretical Methods

3.1 CFD Numerical Approach

In this study, CFD simulations are used as the main approach to investigate the dynamic process of liquid cone-jet generation. CFD solutions for current EHD problem can be considered as a balance between the hydrodynamic forces and electrostatic forces. In this model, there are no assumptions made for the initial shape of the Taylor cone or charge distribution along the liquid surface. All the liquid deformations and the changes in charge distribution are due to the forces, including the applied electric field. The simulation work was carried out using the ***FLOW-3D*** commercial CFD software package (version 9.4, Flow Science Inc., Santa Fe, NM) [68]. It is an all inclusive CFD software package for accurate fluid modeling in a wide variety of applications. Its user-friendly interface allows for model setup, and for post-processing of results using all kinds of visualization tools for further investigation.

The application of CFD tools to test ESI emitter designs is novel and there has been very limited work reported so far [51, 55, 67]. In my opinion, this is largely due to the fact that the traditional CFD methods are mainly developed for simulations within the mechanical engineering realm, where phenomena are mostly on a macro-scale. Thus CFD is barely used for analytical research, especially for nano-scale emitter designs. Though challenging, the benefits of taking advantage of CFD tools for emitter development are many:

First, a CFD model can describe the whole dynamic generation of the cone-jet. A wealth of information about the shape of the liquid cone-jet, liquid flow, electric field, charge distribution and force distribution, is obtained and all these parameters change with time.

Second, CFD simulation provides us with an ideal virtual lab that enables control over the physical process, and isolates specific phenomena for investigation. As mentioned before, several critical parameters in the experiments play a role in the electrospray process. It is difficult to keep consistency in the physical condition between studies. Under the ideal physical condition of CFD modeling, the comparison between runs is much more reliable and convincing.

Finally, CFD tools make emitter design much more efficient and cost effective. It can quickly answer many 'what if' questions even before physical prototyping and testing. A change in the physical conditions is just several seconds to achieve for the model, while preparing for the experiments could be tedious.

3.2 Cone-jet Numerical Model

The focus of our simulation was on the stable cone-jet mode. The aim is to investigate how different emitter parameters affect the cone-jet performance and to assess the controllable operating window. Further break-up of jet and the spray of ions were thus not considered. In ***FLOW-3D***, the EHD process of the cone-jet forming is simulated based on LDM implemented in a well-established multi-phase hydrodynamics code [80].

3.2.1 Governing Equations for Fluid Flow

The simulation for flow field is formulated by solving the continuity and momentum conservation laws. Two phases are involved: the gas phase (air) acts as an insulator and the liquid phase (spray solution) acts as a leaky dielectric. Assuming the liquid to be incompressible (of constant density), axisymmetric, Newtonian (of constant viscosity) and laminar, the mass conservation of the whole domain can be expressed as,

$$\nabla \cdot \vec{v} = 0 \tag{3.1}$$

where $\vec{v}$ is the flow velocity, $\nabla \cdot$ is the divergence. Equation (3.1) means that the local volume dilation rate is zero, which ensures the continuous fluid flow. To take into account also the surface tension on the liquid-gas interface, electrical stress and gravitational acceleration, the Navier-Stokes equation governing the motion of liquid can be expressed as,

$$\rho \frac{d\vec{v}}{dt} = -\nabla P + \eta \nabla v^2 + \overrightarrow{f_e} + \rho \vec{g} \tag{3.2}$$

where $\nabla \cdot$ is the divergence, P is the fluid pressure, $\overrightarrow{f_e}$ is the electromechanical force, η is the viscosity coefficient, g is the gravitational acceleration. The left side of the equation describes acceleration, and may be composed of time dependent or convective effects. The right side of Equation (3.2) is in effect a summation of forces. The pressure gradient ∇P is given by normal stresses that turn up in almost all situations, dynamic or not. The second part describes viscous forces and, for incompressible flow, this is only a shear effect. The fourth part is due to gravity.

The EHD coupling is achieved via an additional source term, which is the third part. This electrical volume stress $\overrightarrow{f_e}$ can be derived as [81]:

$$\overrightarrow{f_e} = q\vec{E} - \frac{1}{2}\vec{E} \cdot \vec{E}\nabla\varepsilon \tag{3.3}$$

where $\vec{E}$ is electric field, ε is the permittivity of the fluid, and q is the net free charge density near the interface. The first term on the right in Equation (**3.3**), known as the Coulomb force, is the strongest EHD force and is the force per unit volume on a medium containing free electric charge. The second term on the right is due to polarization stress, and acts in the normal direction of the interface as a result of the term$\nabla\varepsilon$. Since LDM assumes that the electric charges are only located at the interface, both the Coulomb force and polarization effect are exerted on the interface. The advantage of putting Equation (**3.2**) this way is that it isolates all the electromechanical effects on the hydrodynamics as an additional force [66].

3.2.2 Governing Equations for Electric Field

Along with the hydrodynamic equations presented above, the Laplace equation governing the LDM, the electro-quasi-static assumption within the liquid cone-jet is introduced, negligible bulk free charge density is assumed, and the electric field is considered to be irrotational and divergence-free within the computational region. Thus the governing equation for the electric field in the bulk fluid region is:

$$\nabla^2\phi = 0 \tag{3.4}$$

where $\boldsymbol{\phi}$ is the electric potential. At the fluid-air interface, free charges carried by conduction and bound charges subjected to polarization exist. The charge conservation law determines the accumulation rate of free charge at the interface,

$$\frac{\boldsymbol{dq}}{\boldsymbol{dt}} = -\vec{\boldsymbol{n}} \cdot \boldsymbol{\sigma}(\boldsymbol{\nabla\phi}) \tag{3.5}$$

where $\boldsymbol{d/dt}$ is the Lagrangian derivative, $\boldsymbol{q}$ is the interfacial charge density and $\boldsymbol{\sigma}$ is the electrical conductivity of the liquid. The vector $\vec{\boldsymbol{n}}$ represents the direction normal to the interface. The presence of the interfacial charge density then creates an electric field discontinuity in the direction normal to the interface while at the same time maintains the conservation of current in the tangential direction.

$$\vec{\boldsymbol{n}} \cdot (\boldsymbol{\varepsilon_l \nabla\phi_l} - \boldsymbol{\varepsilon_m \nabla\phi_m}) = \boldsymbol{q} \tag{3.6}$$

$$\vec{\boldsymbol{t}} \cdot (\boldsymbol{\varepsilon_l \nabla\phi_l} - \boldsymbol{\varepsilon_m \nabla\phi_m}) = \boldsymbol{0} \tag{3.7}$$

where $\vec{\boldsymbol{n}}$ is the unit normal to the surface, $\vec{\boldsymbol{t}}$ represents either of the two orthogonal tangent vectors embedded in the surface, and $\boldsymbol{\varepsilon_l}$ and $\boldsymbol{\varepsilon_m}$ are permittivities of liquid and the medium, respectively.

3.3 CFD Modeling Strategy with *FLOW-3D*

3.3.1 Free Gridding System and *FAVOR* Technique

Gridding refers to the subdivision of the computational region into a set of small control volumes and it is usually a rather tedious task. The choice for the best grid system depends on many

factors: the convenience in generation, memory requirements, numerical accuracy, flexibility to conform to complex geometries, and flexibility for localized regions of high or low resolution. In ***FLOW-3D***, a good balance is employed with a unique free gridding method [82]. Different from most CFD programs that employ geometry conforming grids; in this case, the operation of geometry building and grid generation are independent. The significant advantage lies in the fact that changes in either the grid or geometry can be made freely without requiring changes in the other.

When geometry is imported, the first step is for the preprocessor to place the geometry into the computational grid. The platform is based on a structured finite difference grid with simple rectangular grid used. The grid is staggered so that scalar quantities, such as temperature and pressure are computed at cell centers, and vector and tensor quantities are computed at cell faces (Figure 3.1).

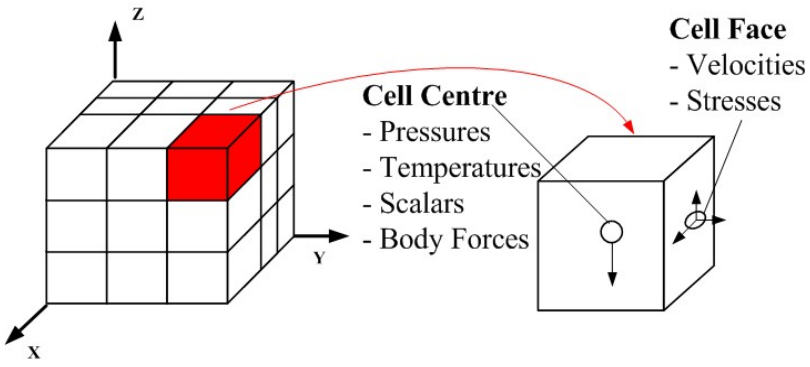

Figure 3.1 Illustration of finite difference grid with rectangular cell

A rectangular element has the advantages of ease of generation, regularity for improved numerical accuracy. Solid geometry is then accurately defined by introducing a Fractional Area Volume Obstacle Representation (*FAVOR*) [82]. Figure 3.2 is an illustration of the method. In this technique, the geometry is embedded by computing which cells are blocked, which are open and which are fractionally blocked. Two quantities are computed to define the geometry within each element: Volume Fractional (VF) of each cell volume and Area Fraction (AF) of each cell surface.

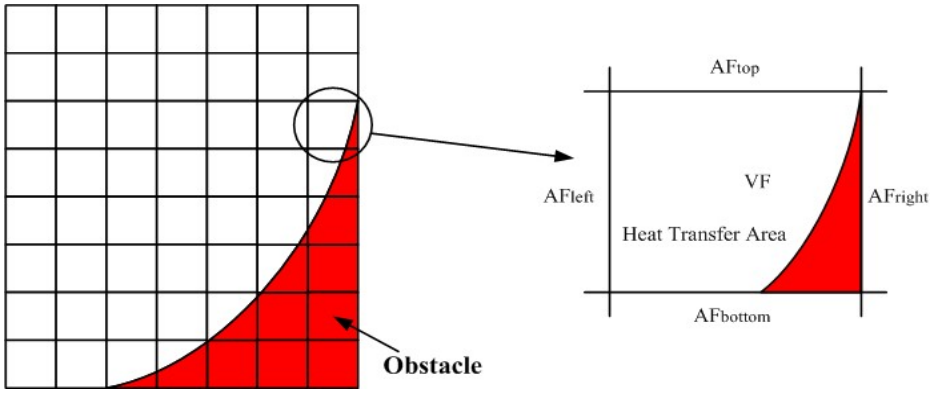

Figure 3.2 Fractional area/volume object representation

With the *FAVOR* technique, the generation and modification of grids and geometries can be done easily for users. It is an automated computing process that will simply calculate the intersections between a grid and an obstacle. Moreover, a traditional mesh requires each cell to be either entirely blocked or entirely filled when describing the objects. This becomes the main limitation associated with simple rectangular grid since discrete steps would normally appear at the boundaries. This introduces flow losses and other undesirable effects. The problem becomes

more significant when it is used to accurately model complex geometries with curved shapes. With *FAVOR*, the 'stair-stepping' effect is eliminated by smoothly blocking out fractional portions of grid cell faces and volumes [83]. The location of the interface in each cell is defined as a first-order approximation- a straight line in two dimensions and a plane in three dimensions, determined by the points where the obstacle intersects the cell faces [84]. This method replaces all obstacle surfaces, curved or not, with short, straight-lined segments and give an efficient description for the obstacle. A comparison to the traditional grid method in describing the same obstacle region is shown in Figure 3.3. The *FAVOR* technique only needs 7 bins to achieve accurate description，while a traditional mesh generation technique requires many more. Given this fact, it should still be noted that, to achieve an adequate accuracy in reproducing a curved surface, smaller size cells and a finer mesh are still required.

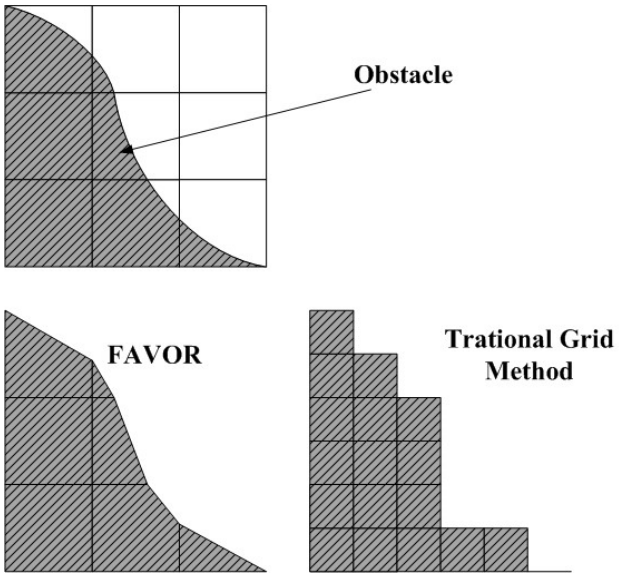

Figure 3.3 Comparison of effectiveness between *FAVOR* and traditional grid methods.

3.3.2 Free Surface Tracking and VOF Method

The physical process of cone-jet formation is a typical free surface problem. “Free" arises from the large density difference across the interface of the two phases (e.g.1000:1 as for water and air). In such cases, the liquid can be assumed to move freely without constraint from the gas. The modeling strategy in ***FLOW-3D*** is to assume the velocity in the gas phase is small so that its impact on the denser fluid is only a constant pressure, and the momentum equations do not need to be solved there, saving lots of computational effort.

In CFD field, free surface problems are notoriously complicated to simulate since it often involves free surfaces in complex geometry that are in many cases, highly transient. The difficulty is often referred to as the ‘classic mathematical free-boundary problem’ [85]. On one hand, the solution region changes with moving free surface, and on the other hand, the motion of the surface will, in turn, be determined by the solution. What’s worse, the changes in the solution region include not only the size and shape, but also the coalescence or break up of regions (i.e., the loss and gain of free surfaces). To numerically solve the rapidly varying flow during the cone-jet formation process, it is important that the free surface be accurately tracked. Tracking involves three parts: locating the surface, defining the surface as a sharp interface between two phases and applying boundary conditions at the interface.

In ***FLOW-3D***, tracking of the moving fluid surface is achieved with the Volume of Fluid (VOF) technique, which was first developed by Dr. C. W. Hirt [80]. The basic idea of VOF

technique is to introduce the special function F to represent, in each grid cell, the fractional portion of the cell volume that is occupied by liquid, as shown in Figure 3.4.

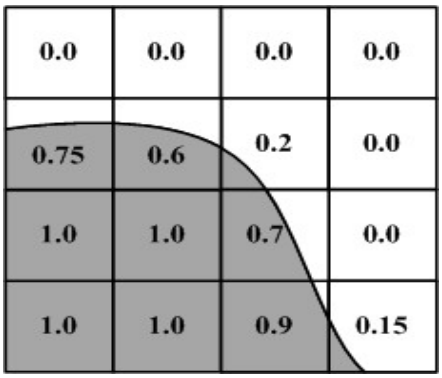

Figure 3.4 Typical values of the VOF function near free surface

The value of F must be between 0 and 1. It is similar to the *FAVOR* method in defining cells that are empty, full, or partially filled with fluid. In interior regions of liquid, the value of F is 1.0; outside of the liquid (e.g. air) this value is zero; and free surface is located in cells where F has a value between 0 and 1, based on the percent volume that is occupied (Equation (3.8)).

$$F(x,y,z,t) = \begin{cases} \mathbf{0} & \textit{outside the liquid} \\ \mathbf{1} & \textit{inside the liquid} \\ \mathbf{>0, <1} & \textit{on the free surface.} \end{cases} \tag{3.8}$$

A surface angle and a surface location in the neighboring cells are used to define the slope of the free surface at the boundary. Once again, similar to *FAVOR* method, an exact capture for fast changes in the free flow surface would inevitably require a finer grid to be applied. To represent also the dynamic nature of the interface, F has to fulfill the basic kinematic equation below:

$$\frac{dF}{dt} + \vec{v} \cdot \nabla F = 0 \tag{3.9}$$

where $\vec{v}$ is the velocity of the fluid.

VOF approach offers a natural way to efficiently examine free surfaces and their evolution, in which it only requires to assign another numerical value (F) to each grid element which is consistent with the recording of all other fluid properties in an element such as pressure and velocity components.

3.3.3 Workflow of CFD Simulation

A typical workflow for CFD modeling with ***FLOW-3D*** consists of three stages: Pre-processing, equations solving, and post-processing.

- **Pre-processing**

The pre-processing stage defines the physical problem. It works first on the created model by dividing the region of interest into a large number of control volumes in which average values of flow variables can be stored. In ***FLOW-3D***, models could either be built within ***FLOW-3D*** software package or imported from other graphics software, e.g. AutoCAD. Great care should be taken when constructing the mesh since it critically determines the quality of the flow solution. An adequate mesh is required to accurately resolve the geometry as well as to capture the expected flow region.

Figure 3.5 Iteration approach for geometry design and mesh building.

Figure 3.5 shows an example of a typical meshing procedure of a tapered-emitter electrospray. Considering the symmetry characteristics of the single-channel model, a cylindrical mesh covering 30 degrees of the computational area is applied for better computational efficiency. After applying the mesh, the '*FAVOR*' option allows users to visualize how accurately the computational region of interest is resolved under the current mesh. In order to better capture the thin jet region of the flow, a finer mesh is applied at the centre area (as a side view of the mesh, see Figure 3.6. A mesh sensitivity test may be still needed in a later simulation stage to find a balance between computational efficiency and a reliable result.

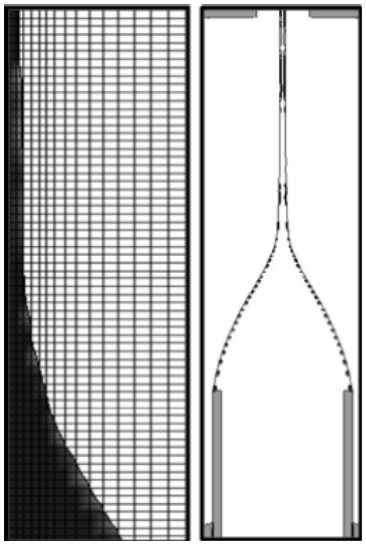

Figure 3.6 (Left) A close-up view of the jet region with mesh superimposed to show resolution. (Right) The horizontal shape of the Taylor cone and emitter plotted together with the contour lines of the charge density distribution.

When a computational region is settled, properties for solid construction (emitter) and fluid flow are carefully assigned according to real-world experimental conditions. In my simulation, high electric potential is applied only to the solid capillary and the spraying liquid is considered to be viscous, incompressible, and laminar flow. The physical and electrical properties of the liquid are assigned as follows [51]: density ρ = 1030 kg/m^3, viscosity = 0.008 Pa·s, surface tension coefficient = 0.037 N/m, dielectric constant = 55, electrical conductivity = 135×10^{-6} S/m. Boundary conditions are also specified around the computational block to define the initial state of the flow and the physical environment. As an illustration, boundary conditions for a single-nozzle emitter case are set with reference to Figure 3.7: Boundary 1 (inflow boundary): Velocity boundary condition where the inlet flow rate towards downstream from the emitter tip $\boldsymbol{U}_z$ was

defined; Boundary 2: No slip boundary for the inner wall of the capillary where the velocity $\boldsymbol{U}_z$ at the liquid-solid contact line is zero. Boundary 3, 4: Symmetry boundary condition was defined for computational surfaces parallel to axis to assure no flow or heat transfer across the boundary plane. Boundary 5 (outflow boundary): Continuative boundary condition was chosen to represent a spatially steady flow condition by forcing all physical variables (steady flow) to be constant when fluid passing the boundary.

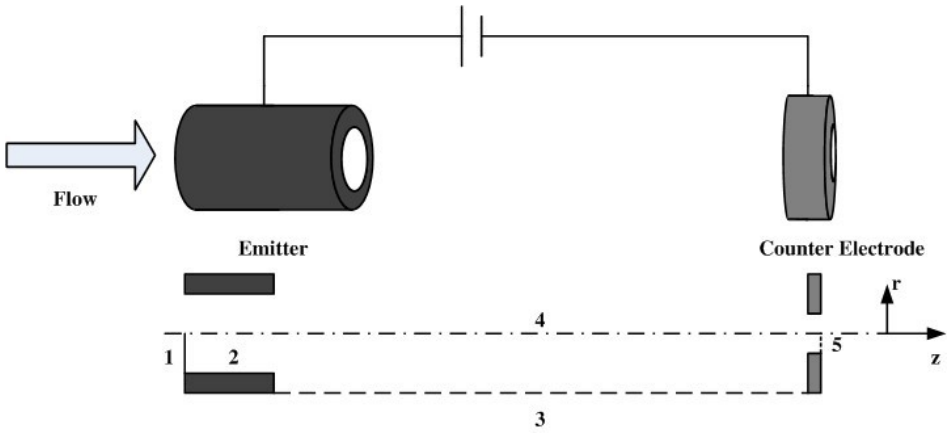

Figure 3.7 Boundaries of the computational region for a typical electrospray simulation.

- **Obtaining a Flow Solution**

After the first stage, the characterization and definition of the physical problem to be simulated are completed. All the involved equations are then solved numerically yielding a complete picture of the flow down to the resolution of the grid, by the chosen solver. Numerical algorithms representing approximations to the conservation laws of mass, momentum, and energy are then used to compute these variables in each control volume. The computational cycle involves the integration of the governing equations over each cell, the conversion of resulting integral

equations into algebraic equations and the solution of algebraic equations by an iterative method. It is generally the most time consuming step, and depending on the scale of the computational region and mesh resolution, it could take from several hours to weeks long.

Monitoring the simulation is easily achieved by watching the simulation panel from which the progress and accuracy of the simulation can easily be seen. A typical simulation panel is shown in Figure 3.8.

Run-time diagnostics allows us to investigate the change of important flow parameters instantly updated in time and to make quick responses. For example, when the mean kinetic energy of the fluid becomes stable, the problem can typically be considered to reach the steady state. Warning messages will usually appear during simulation to report on any computational errors confronted. When this occurs, we need to go back to preprocessing stage to either adjust the mesh or change any unrealistic physical parameters.

Another more direct way to monitor the simulation in ***FLOW-3D*** is to render and visualize the electrospray movie with instant simulation results during the procedure. Figure 3.9 shows the interface of rendering graphical results during simulation. By selecting a certain time step on the right, the corresponding computational result will be presented through visualization on the left. This helps us to quickly evaluate the advance of simulation.

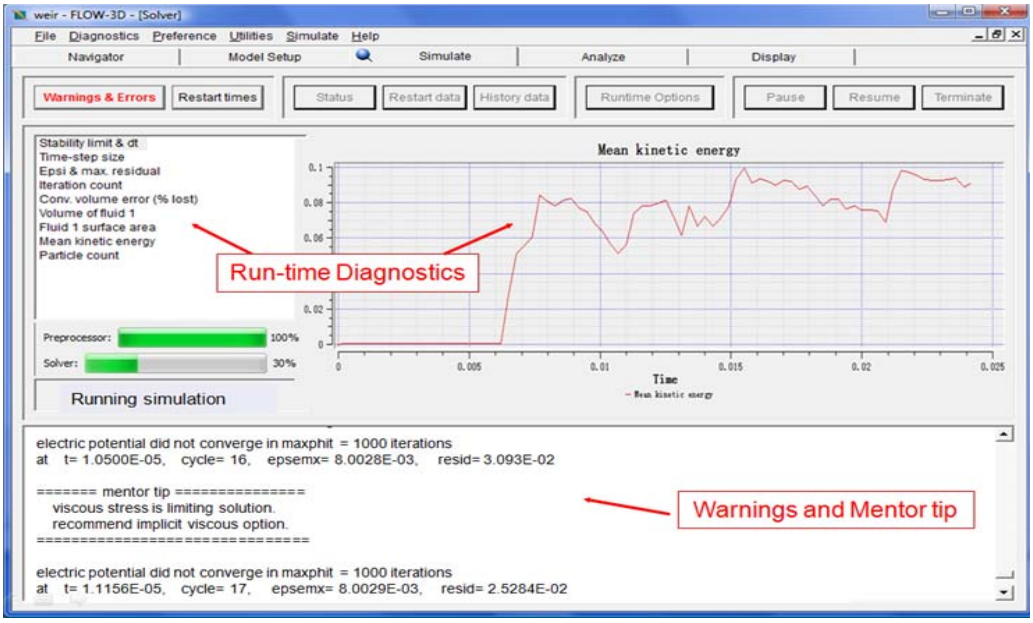

Figure 3.8 Typical interface of simulation panel during simulation process.

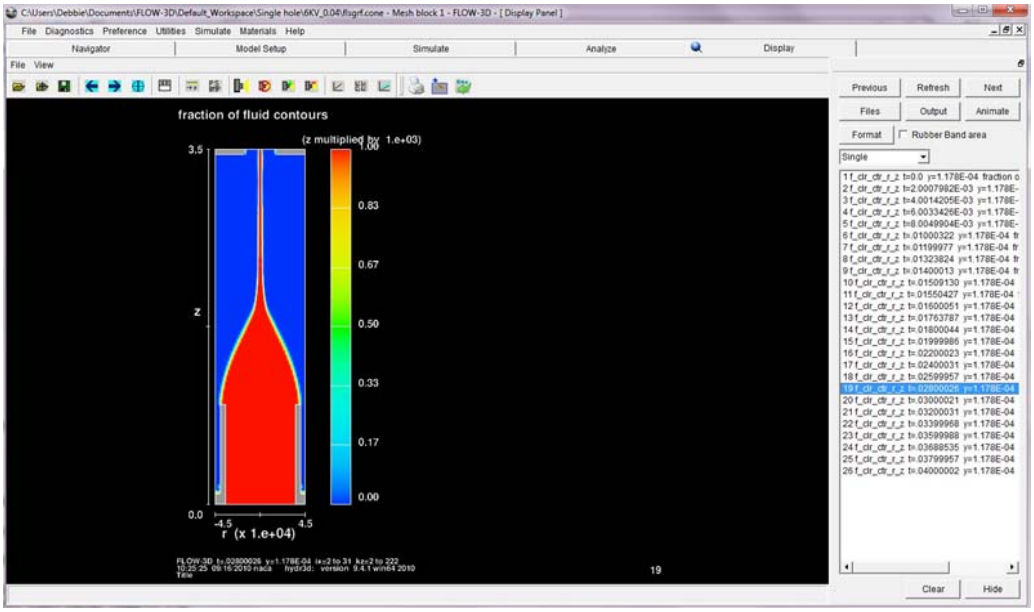

Figure 3.9 Typical panel for displaying instant simulation result during simulation process.

- **Post-processing**

Post-processing involves the organization and interpretation of the calculated flow data and the generation of CFD images and animations. With ***FLOW-3D*** post-processing tools, computational results can be reported in many different ways: text files with data for quantitative data analysis, 1D, 2D, 3D plots, or movies. In our simulations, quantitative analysis for spray current is performed to determine the quality of electrospray and the performance of the emitter used. The calculation for spray current of the jet will be discussed later.

3.3.4 Spray Current Calculation

In LDM, charges are transported in two ways under the effect of the electric field. At the base of the liquid cone, charges are mainly transported by conduction to the liquid-air interface. The tangential electric stress at the interface then drives these interfacial charges toward the cone apex together with the surrounding liquid and causes the convection flow. As a result, the current through the cone-jet equals the sum of these two contributions[64].

$$I = I_{cond} + I_{conv} = \pi R_s^2 \overrightarrow{E_z} \sigma + 2\pi R_s \overrightarrow{u_z} q \tag{3.10}$$

where I_{cond} and I_{conv} are the conduction and convection current, respectively, R_s is the jet radius, $\overrightarrow{E_z}$ is the electric field on the surface of the jet along the z-direction, $\overrightarrow{u_z}$ is the axial velocity of the jet and q is the surface charge density.

The data needed for the calculation can be generated from the postprocessor of ***FLOW-3D*** after simulation. Electric surface charge density was not included in the original version of the

software but was customized as a new output result. In Equation (3.10), all the parameters of interest are located in the surface region. Since the output file generated from ***FLOW-3D*** involves all time steps and all points throughout the computational area, *FORTRAN* programs were specially developed to filter and process the huge number of output files (only focus on points where F is between 0 and 1) and make a statistical average over time and space.

Chapter 4 Experimental Investigations and Measurements

In this chapter, offline electrospray experiments are performed with the commercial single-channel emitter, a 2-hole pulled glass MSF and a fabricated 3-hole polymer MSF. The nanoelectrospray behavior is clearly imaged under a microscope during the experiments. The quantitative results of the spray current are obtained from offline electrospray experiments. The experimental results and investigation will be used to validate the CFD simulation. Part of the work from this chapter regarding multi-spray experiments was cited from paper in press[86].

4.1 Commercial Single-aperture TaperTip

The influence of flow rate and voltage on the electrospray behavior and performance were systematically evaluated via microscopic imaging and spray current measurement. Rational operational parameters were found for this type of emitter to operate electrospray within the stable Taylor cone-jet mode.

4.1.1 Impact of Flow Rate

Figure 4.1 shows the offline electrospray images taken by continuous infusing of the sample solution (50% water and 50% methanol, containing 1% acetic acid) at constant electric potential of 1.5 kV. The trend shows an increase in the emission zone with growing flow rate. The Taylor cone profile gradually becomes less visible at 20 nL/min and no cone could be generated below this point.

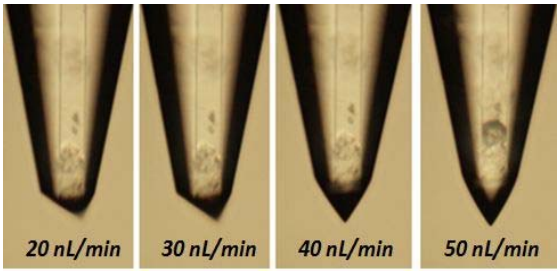

Figure 4.1 Taylor-cone shape at flow rate from 20 nL/min to 50 nL/min (left to right) under a constant electric potential of 1.5 kV.

The corresponding electrospray TIC was measured during the stabilized electrospray. The evolution of spray current under different flow rates was traced for 1 minute long and the result is shown in Figure 4.2 (A). The relative standard deviation (RSD) for the measurements shows the increasing instability of the electrospray with reduced flow velocity. According to Fernandez de la Mora *et al*. [40], inside the stability island of the electrospray, the current emitted from a Taylor cone does not depend on the applied voltage but scales with the square root of the flow rate. The averaged spray current with varied flow rate is plotted in Figure 4.2 (B) and the trend is consistent to the square root law. Obtaining more points for spray current over a wider range of flow rate would be better to compare with the scaling law, while current experimental condition limits the flow rate to be applied outside the range of 20 nL/min to 50 nL/min. A lower flow rate will lead to significant wetting at the emitter tip where stable cone-jet could not be operated, and at a higher flow rate, big droplets will be easily accumulated on the counter electrode plate and strongly interfere with the whole electrospray process.

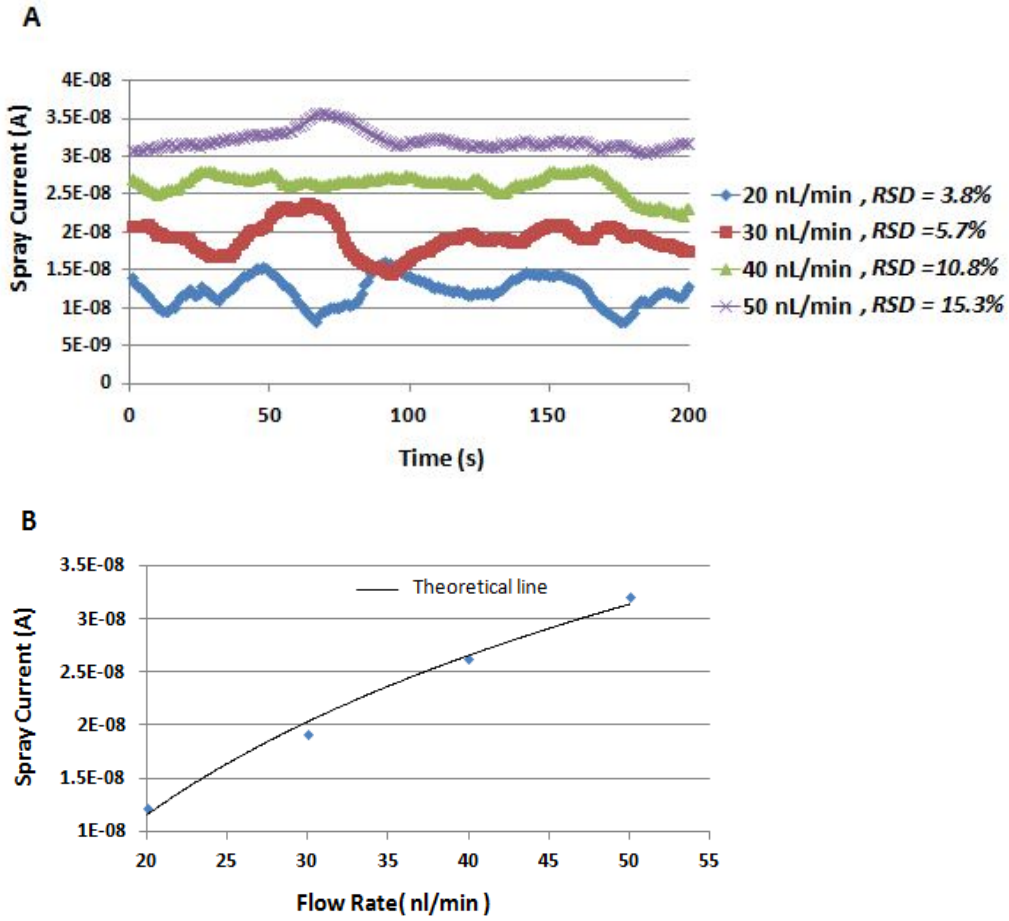

Figure 4.2 (A) Time evolution of spray current under flow rate from 20 nL/min to 50 nL/min with the same applied potential of 1.5 kV; (B) Plot showing square root dependence of spray current and flow rate from 20 nL/min to 50 nL/min

4.1.2 Impact of the Applied Voltage

Systematic experiments were also performed to test the impact of the applied electric potential on ESI performance. Figure 4.3 (A) shows the observations of Taylor cone-jet morphologies obtained by gradually increasing the voltage from 1.3 kV to 1.9 kV, at a constant flow rate of 50 nL/min. The corresponding spray current measurements are plotted in Figure 4.3 (B). Several

distinctive regimes show up during this process (we use the suggested nomenclature [87] for the description): A wetting-pulsating regime started first at 1.2 kV in which the liquid wets the outside of the emitter and a large droplet is firmly anchored to the emitter rim, the current then increases with the voltage up to 1.3 kV. The spray current remained constant despite a voltage increase. An astable regime was observed at 1.7 kV where pulsating and cone-jet mode underwent periodic switching, a large increase in spray current is observed for the latter mode. A Taylor cone was stable after 1.8 kV where stable cone-jet mode was attained.

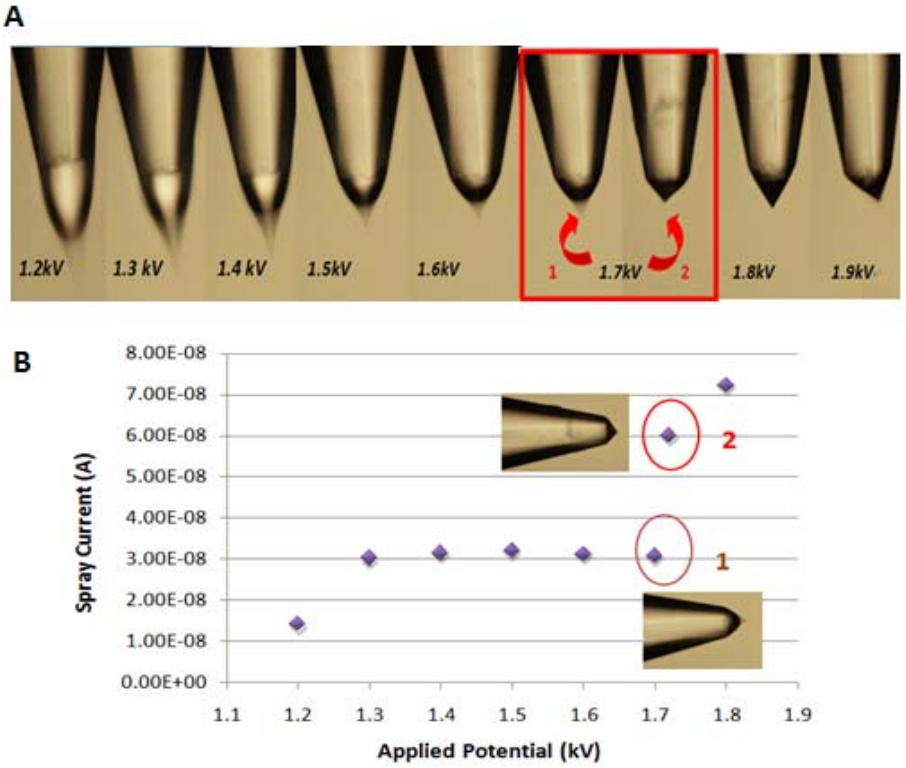

Figure 4.3 (A) Offline electrospray images under electric potential from 1.2 kV to 1.8 kV at a constant flow rate of 50 nL/min. (B) Spray current as a function of applied potential from 1.2 kV to 1.8 kV under constant flow rate of 50 nL/min.

4.1.3 Characterization of Emitter

Throughout the experiments, the commercial tapered tip showed good robustness, reproducibility and resistance to clogging. The base of the Taylor-cone was always anchored to the outer rim of the capillary.

The characterization of nanoelectrospray with thecommercial single-nozzle emitter was further conducted with a wider range of parameters. The lowest practical flow rate is found to be 20 nL/min. However, due to the limited distance in this experiment-only 1mm from emitter tip to counter electrode, we are unable to operate electrospray at a flow rate higher than 60 nL/min. At a high flow rate, the time is too limited for droplets to become ions, and a stream of tiny droplets results in a progressively growing drop on the counter electrode plate, which is clearly visible during experiments. When this occurs, the convex meniscus of the drop on the end plate would not only further shorten the distance between the emitter tip and the counter electrode, but also change the uniformity of the electric field. The effect introduces instability and oscillation in the electrospray process along with a significant drop in the collected spray current.

The results from experiments conducted between flow rates (20 nL/min to 60 nL/min) and electric potentials (1.2 kV to 1.9 kV) provide a clear picture of the optimal operational parameters to obtain a stable Taylor-cone jet mode (Table 4.1).

From Table 4.1, we can see that, for the emitter used, the most optimal parameter for generating stable electrospray is at a flow rate above 40 nL/min where the cone-jet mode can be

stabilized within a wider range of the applied potential. Under such experimental conditions, the electrospray was seen to be stable for several hours.

Table 4.1 Impact of Flow Rate and Applied Potential on Electrospray Domain

Flow Rate (nL/min) / Potential (kV)	20	30	40	50	60
1.2	P[1]	P	P	W-p[2]	-[3]
1.3	P	P	P	P	-
1.4	P	P	P	P	-
1.5	P	P	C-j[4]	P	-
1.6	P	C-j	C-j	P	Astable (P&C-j)
1.7	-	C-j	C-j	Astable (P&C-j)	C-j
1.8	-	-	-	C-j	C-j
1.9	-	-	-	-	C-j

[1] P: Self-regulating pulsating regime

[2] W-p: Wetting-pulsating regime

[3] -: No regime available

[4] C-j: Cone-jet regime

4.2 Two-aperture Glass MSF Emitter

Offline experiments were conducted for 2-hole pulled glass MSF emitter. Figure 4.4 shows a successful multi-spray with this emitter by infusing the liquid at a flow rate of 200 nL/min. It is obviously seen that instead of forming two straight jets, the sprays point away from one another. This is due to the fact that the two positively charged jets are not separated enough to avoid the Coulomb repulsion from each other. Also, it was found that for generating multi-spray with this type of emitter, a high electric potential, 4000 V, is required. At lower voltages, the spray

coalesces into one larger cone, or does not form a cone at all. The observed spray current is very low and unstable, which is not ideal for use in ESI-MS application.

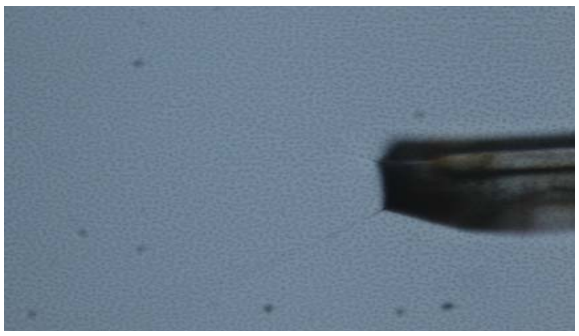

Figure 4.4 Multi-spray of a two-channel pulled-glass fiber under microscope.

4.3 Three-aperture MSF Emitter

Offline experiments were conducted for a polycarbonate 3-hole MSF emitter to test its feasibility to achieve MES. Without any hydrophobic treatment, the stable MES was sustained about 30 minutes. For the untreated MSF, the experimental requirement to achieve MES was rather strict. Only a limited voltage ranging from 3500 to 4000 V could be used. A higher potential would cause arcing, and lower voltages would result in the significant wetting at the tip from different channels and they tend to coalesce easily to produce a single large cone. The optimal flow rate to achieve stable MES was found to be within 40 nL/min to 60 nL/min.

Figure 4.5 shows the Taylor cone images captured under microscope during the MES with untreated a 3-hole MSF emitter. The evidence proved the ability of our simple designs for 3- hole emitter to achieve the true MES. The success should largely be attributed to the radical pattern for the hole design that eliminates the electrical shielding effect. As a result, each channel in the

emitter feels the electric field the same way and they are in equivalent state in generating independent Taylor cone-jets. However, similar to the previous 2-hole emitter electrospray, the Taylor cone-jet captured from the side view of MES is not straightly emitted from each channel; rather they repel each other away toward the outside periphery of the capillary.

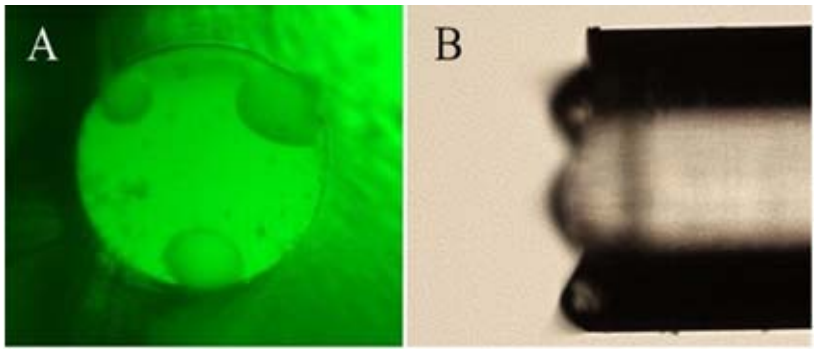

Figure 4.5 (A) Top View: MES on a 3-channel untreated polycarbonate MSF; (B) Side View: MES on a 3-channel untreated polycarbonate MSF with focued on far Taylor cones[86]

The main issue that prevents the stable MES is the significant high wettability of the emitter tip. It is rather important to keep the fiber head as dry as possible at the very beginning in order to achieve independent MES. Sometimes measures like physically drying the head of the MSF, or blow with compressed air are needed between starting the pump and turning on the electric voltage. This not only affects the spray current but also the stability of the electrospray. Because the Taylor cone base is not restricted to the i.d. of the channel, the physical distance between electrosprays is shortened and the interference from Columbic forces is not completely avoided. In order to design emitters containing channels that would allow as many independent nanoelectrosprays as possible on the single fiber tip, further effort is needed to prevent surface wetting and prevent coalescence of the initial droplets.

Chapter 5 CFD Simulation and Numerical Analysis

In this Chapter, the computational results from CFD simulations of electrospray will be presented. Starting with a validation test on a macro-scale emitter, we performed a full scale characterisation of the electrospray process. The stability island of the cone-jet mode under different conditions was investigated and the results were used to further study the effect of the applied potential and fluid velocity on the final spray current. The advantages of CFD simulation for the current research area are clearly demonstrated and many interesting detailed phenomena of the electrospray process which are hard to achieve empirically are accessed.

5.1 Validation Test for Electrospray with Macro-scale Emitter

The prototype of the electrospray apparatus chosen for the validation test is similar to the example shown in a ***FLOW-3D*** technical paper [88], in which the results were used to show the capability of ***FLOW-3D*** to describe electrospray. The performance was further investigated and evaluated by studying its response to various parameters like emitter design, flow rate, and the applied electric potential.

5.1.1 Validation Model

A schematic diagram of the ESI setup is illustrated in Figure 5.1. A flat-tip emitter for spraying is represented by a uniform nozzle with an i.d. of 0.7 mm that is charged to 6 kV. Downstream 2.5 mm there is a grounded plate perpendicular to the axis of the emitter with a central hole with a

diameter 0.3 mm. A flow of liquid is continuously driven through the channel at a fixed axial velocity of 0.02 m/s. The properties of the liquid are as follows: density = 827.0 kg/m^3, viscosity = 0.0081 Pa · s, dielectric constant = 10.0, surface tension = 0.0235 N/m and conductivity = 8.05×10^{-6} S/m.

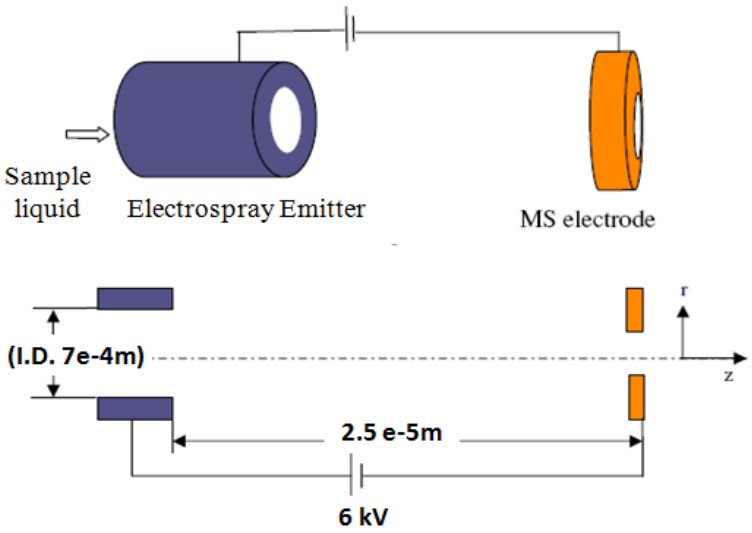

Figure 5.1 Schematic of the ESI model used for the validation test.

For this single-hole emitter model, a non-uniform cylindrical mesh is selected to reduce the computational effort. The mesh consisted of 30 radial cells and 220 axial cells (6600 cells in total). A minimum radial cell size of 0.8×10^{-5} m was used near the axis of symmetry to better capture the fine jet. Boundary conditions for the computational region for this case have been described in Chapter 3.3.3 with reference to Figure 3.7.

5.1.2 Simulation Results

The total time simulated was over 0.08 s. Fluid filled the nozzle, and then gradually rose from the flat tip. The steady state is approached after an extended simulation time of 0.024 s. At later times, the mean kinetic energy is observed to only fluctuate within a 4% range (see Figure 5.2).

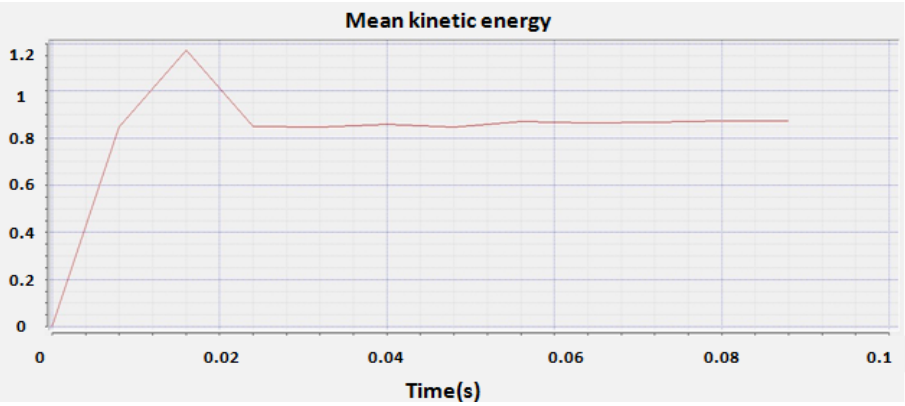

Figure 5.2 Time evolution of mean kinetic energy.

Figure 5.3 shows the time evolution of the electrospray process within the computational domain, together with iso-potential lines indicating the change of the electric field. The initial liquid rises from the top of the nozzle and is gradually drawn out to form a jet. The jet forms rapidly at around t=0.019 s and then slowly evolves to have a smaller diameter as it approaches a steady state condition. The deformation of iso-potential lines indicates that the surrounding electric field is greatly influenced from uniform to non-uniform, during the establishment of the cone-jet mode. The corresponding electric field intensity contours are presented in Figure 5.4. The color variation depicts a large jump in the electric field across the free surface of the cone-jet,

which is responsible for the normal and tangential electric stresses. The normal stress maintains the cone shape and the tangential stress accelerates the liquid towards the jet.

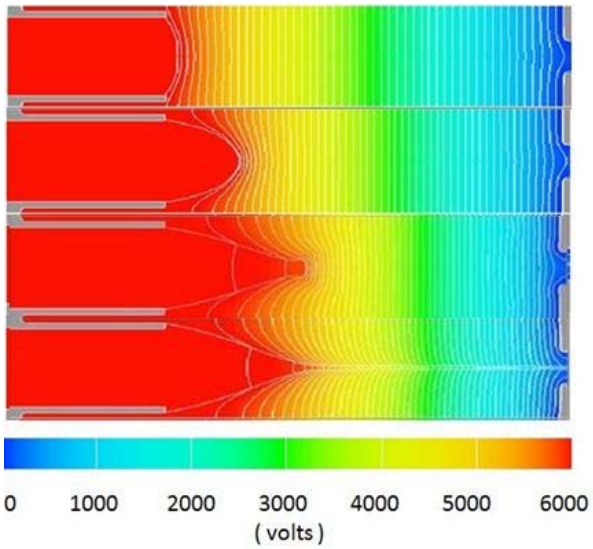

Figure 5.3 Generation of a Taylor cone-jet mode (simulation) plotted with iso-potential lines at times (Top to bottom panels correspond to 0.002 s, 0.012 s, 0.018 s, 0.08 s respectively).

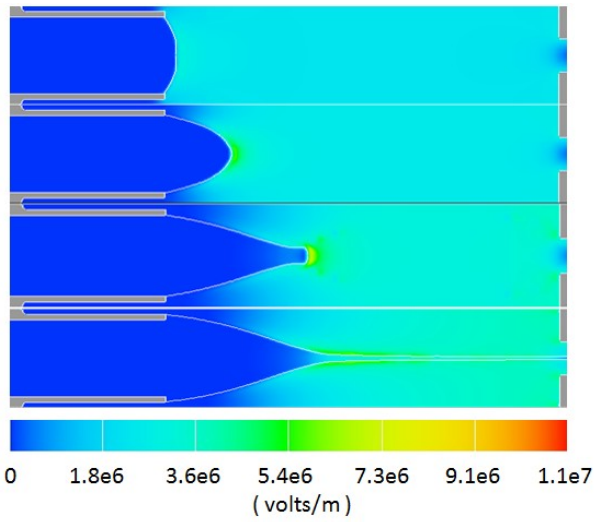

Figure 5.4 Electric field corresponding to Figure 5.2 at various times (Top to bottom panels correspond to 0.002 s, 0.012 s, 0.018 s, 0.08 s respectively)

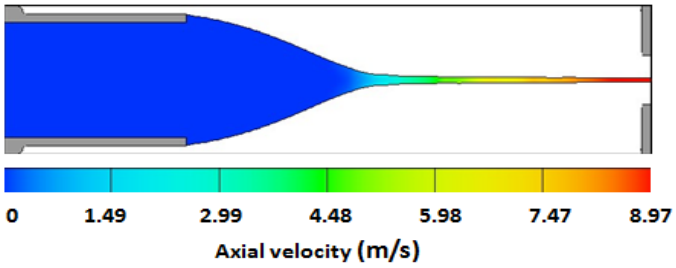

Figure 5.5 Axial jet velocity contours at steady state (t = 0.08 s).

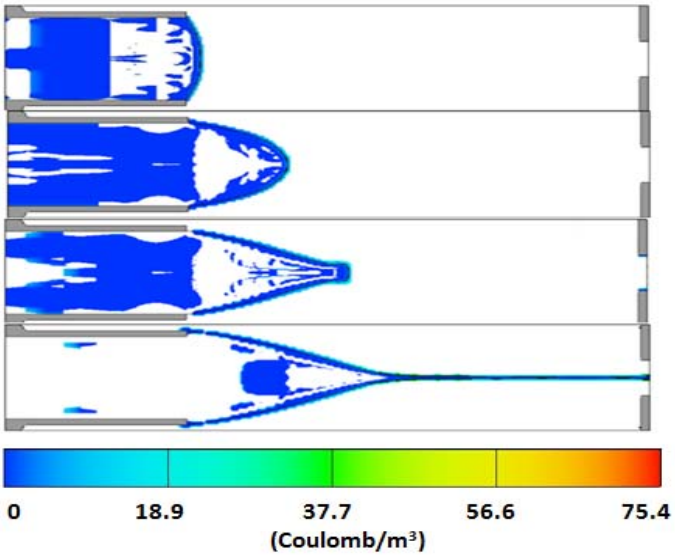

Figure 5.6 Electric charge distributions within cone-jet at various time steps
(Top to bottom panels correspond to 0.002 s, 0.012 s, 0.018 s, 0.08 s respectively)

The jet velocity along the axial direction at steady state is presented in Figure 5.5. As seen in the figure, the liquid is accelerated as it moves along the z-direction due to the action of tangential stresses. The charge density contours within the cone-jet region are shown in Figure

5.6 and as expected, the charge is confined at the liquid-gas interface and there is virtually no charge inside the bulk liquid conforming to the leaky-dielectric model.

5.1.3 Electrospray Characterization

5.1.3.1 Flow Rate and Applied Potential

The cone-jet mode in electrospray has often been described as an island of stability [31, 89-91]. The stability island was found to be critically dependent on two key parameters: flow rate and applied voltage. The relationship between flow rate, applied electric potential and spray performance was investigated to characterize the cone-jet regime.

To investigate the impact of the applied electric potential on electrospray performance, a series of simulations at fixed inflow velocity of 0.02 m/s but with varied applied electric potential were performed. Figure 5.6(A) shows the Taylor cone-jet profiles obtained with 6 kV and 9 kV applied potential respectively. The higher field produces a shorter cone but a larger cone angle at the base of the jet (i.e. cone decreases in size and becomes much closer to the capillary tip). This agrees well with the experimental observations by Hayati et al. [56] where they found that the shear force decreases with increasing voltage while normal stress remains constant, thus thinner jets are produced with larger cone angle. Similar simulations were also performed to study the impact of flow rate and its influence on cone-jet shape (Figure 5.7 (B)). An increase in the flow rate increases the radius of the jet, and the cone is larger and extends toward the counter electrode.

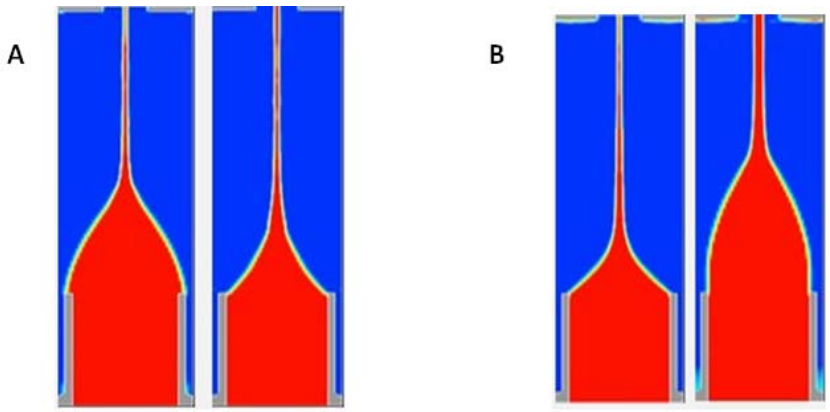

Figure 5.6 (A) Taylor cone-jet profiles under 6 kV (left) and 9 kV (right) potential at 0.02 m/s (B) Taylor cone-jet profiles at 0.01 m/s (left) and 0.04 m/s (right) under 6 kV.

According to Fernandez de la Mora *et al.*[40], the current emitted from a Taylor cone does not depend on the applied voltage and scales with the square root of the flow rate. The current-voltage characteristics predicted by my model are presented in Figure 5.7(A) where spray current increases slightly with the increase in electric potential. The discrepancy might be due to the real physical condition (i.e. stable cone-jet cannot be reached under conditions as such) or numerical error. The good linear relationship in Figure 5.7 (B) between dimensionless I / I_0 and $(v / v_0)^{1/2}$ corresponds well with the expected square root law.

Jet diameter, R, was further calculated at different flow rates and the results are indicated in Figure 5.7(C). The fitted exponential line gives the exponential factor of 0.35, which matches well with 1/3 predicted by Fernandez de la Mora. These simulations indicate that the model is, on the whole, performing according to expectations.

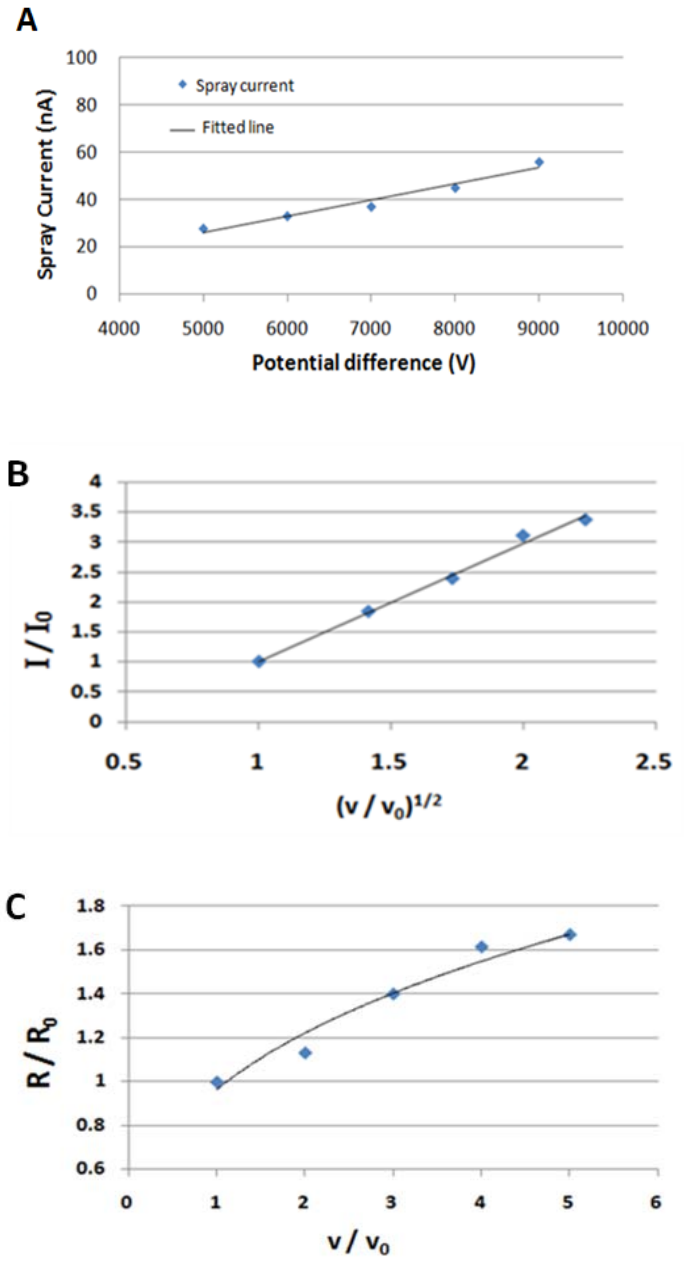

Figure 5.7 (A) Spray current as a function of potential difference under the same flow rate v = 0.02 m/s. (B) Dimensionless spray current ratio (I/I_0) as a function of the square root of flow rate ratio (v/v_0). I_0 is the spray current under the lowest inflow velocity v_0 of 0.01m/s. (C) Dimensionless jet radius ratio (R/R_0) as a function of inflow velocity ratio (v/v_0). R_0 is the jet radius under the lowest inflow velocity of 0.01m/s.

5.1.3.2 Contact angle

As noted previously, the properties of the emitter tip critically determine the morphology of the Taylor cone (base, contact line, shape etc.), which in turn influences the spray performance. Simulations were performed on the same model with modified surface hydrophobicity property and tip geometry. The corresponding cone-jet was investigated and results are shown in Figure 5.8.

For small-scale flows, the surface property of the emitter tip can be an important or even dominant factor. A static contact angle that is between 0 and 90 degrees corresponds to a wetting condition where the fluid will tend to spread out over the surface. Conversely, when the contact angle is between 90 and 180 degrees, the surface is non-wetting, and liquid will tend to bead up. Figure 5.8 (A) shows the tendency clearly, where the left case has a 30 degree contact angle. The base of the Taylor-cone wets to the outer periphery of the emitter. When the contact angle is 20 degrees, the liquid wets all over the emitter tip and no cone-jet could be supported (Figure 5.8 (B)). Due to the symmetric boundary condition (which acts like a mirror) set for the periphery plane in this case, it prevents further spreading of the liquid as observed in Figure 5.8 (B). If complete wetting needs to be considered, this restriction will need to be removed.

5.1.3.3 Impact of geometry of the tip

Parallel simulations were performed on the same emitter design at 20 degrees of contact angle except that a small modification was made to form a tapered tip, Figure 5.8(C). The simulation

results show that the base of the Taylor-cone is always confined to the i.d. of the hole, effectively reduce the wetting.

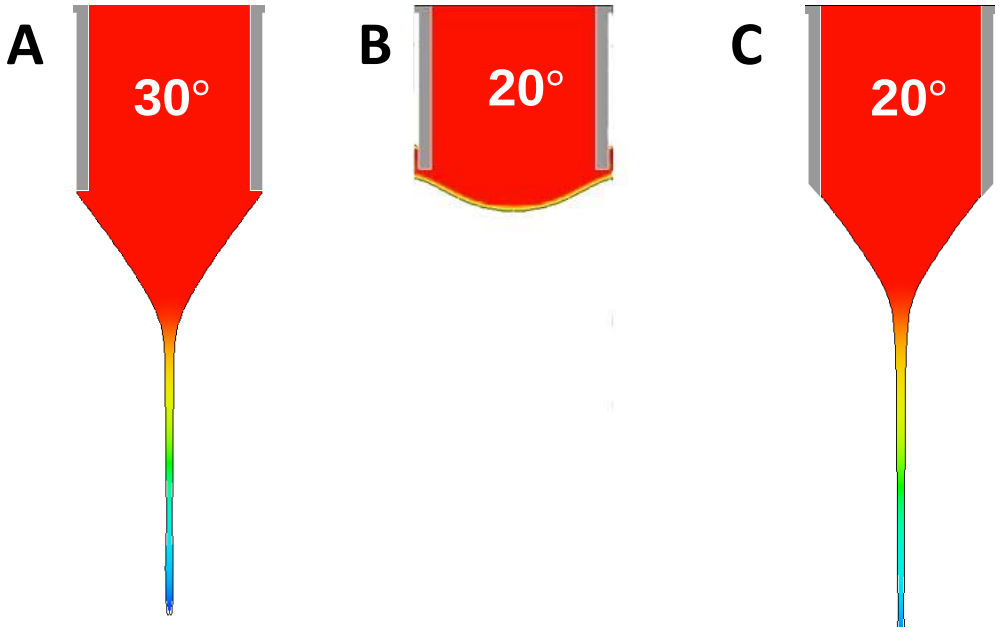

Figure 5.8 (A) Taylor cone-jet profiles with different contact angle of 30 degrees and 20 degrees (B) under the same physical conditions of 6 kV and 0.04 m/s. (C) Cone-jet profile generated from a tapered tip with a 20 degree contact angle at 6 kV and 0.04 m/s (as a comparison with (B)).

5.2 Nano-ESI Simulation with Single-nozzle Emitter

The results in Section 5.1 were for an emitter with a 0.7 mm i.d. nozzle. In experiments, especially in nano-ESI, the i.d. of the emitter used could be as small as several micrometers. As the simulation for electrospray goes down to micro-scale, the computation becomes extraordinarily challenging. The jet becomes a lot thinner and the results are much more sensitive

to the grid applied. Moreover, the numerical stability is greatly disturbed by even a slight change in any physical variables (contact angle, flow rate, property of the spray solution *etc*.) as well as the controllable numerical parameters (computational time step, mesh resolution *etc*.).

Many trials were needed to gain experience with stabilizing the simulation for nanoESI process. First, the sharp change along the free surface of the cone-jet requires the mesh to be as uniform as possible across the transient free surface without causing convergence problems. Second, the computational time step has to be strictly limited to below 3 nano-seconds instead of relying on an automatic time step adjustment, otherwise the computation fails. Finally, a shorter distance between the emitter tip to the counter electrode was used in the simulation, relative to experiment, for computational efficiency and thus the applied electric field required is accordingly much lower.

The successful 1-hole emitter model for micro-scale electrospray simulation had a tapered outside with an i.d. of 20 μm, as consistent with experiment. A high potential is applied to the emitter and, for computational efficiency at this stage, the distance between the emitter tip and the counter end plate, held at ground, was set to 0.25 mm. The properties of the spray solution also conformed to the physical experiments that have been described in Chapter 2.

5.2.1 Mesh Sensitivity Test for Cylindrical Mesh

A well-refined grid is essential for accurately capturing the flow and thus a mesh sensitivity test was carried out on the current model. Parallel simulations were run with different meshes. The

physical condition in the present test is kept consistent where the potential difference is 800 V and the linear inflow flow velocity is 0.09 m/s. An axisymmetric (about Z axis) computational mesh is used considering the symmetric feature of the model. A uniform mesh is chosen to ensure the numerical stability of the free surface flow at micro-scale. All the boundary conditions are the same as set in validation test in Chapter 3.3.3 with reference to Figure 3.7.

A mesh size of 5×10^{-7} m was used as a start in order to properly capture the thin jet. A Taylor cone-jet progressively formed at 0.0005 s and gradually approached to the steady state after 0.001 s. The profile of the simulated cone-jet mode is shown in Figure 5.9 plotted with electric potential contours. The base of the Taylor cone is well confined by the tapered design of the emitter tip which promotes the stability of the electrospray process.

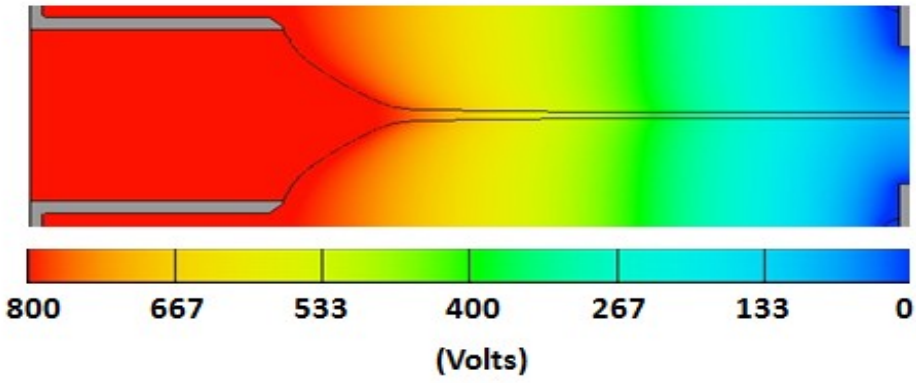

Figure 5.9 Simulated Cone-jet profile generated from micro-scale tapered emitter plotted with electric potential contours.

Figure 5.10 shows the evolution of the mean kinetic energy of the system during simulation. The value is seen to dramatically increase as the Taylor cone-jet generates from the emitter tip and accelerates towards the counter electrode plate. The computation gradually approaches the steady state after 0.015 s when the fluctuations in the mean kinetic energy are less than 5%.

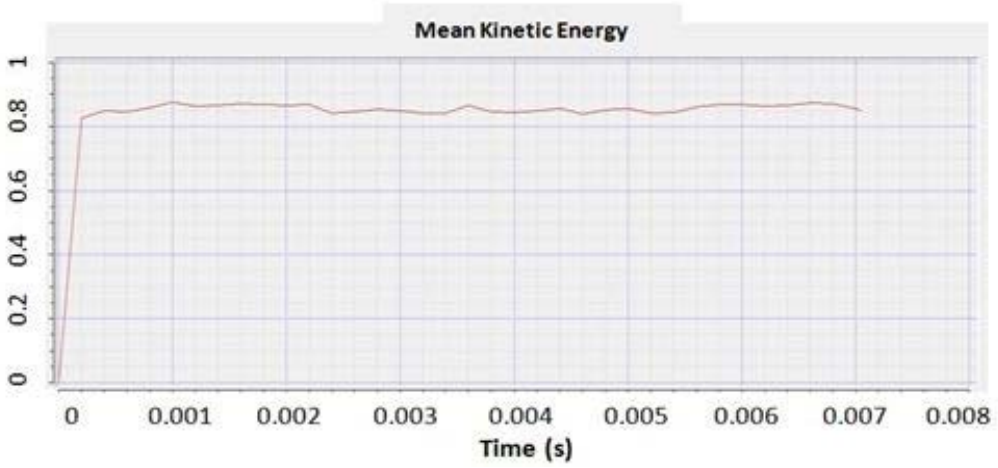

Figure 5.10 The evolution of mean kinetic energy of the simulation system with time.

The steady state of the physical process is further assured by observing no change in jet radius, electric field magnitude, electric charge density, and velocity along the jet with time. Figure 5.11 shows the evolution of the critical flow variables on the jet surface with time, probed at a specific Z-value. All parameters are well converged after 0.015 s conforming to the mean kinetic energy curve.

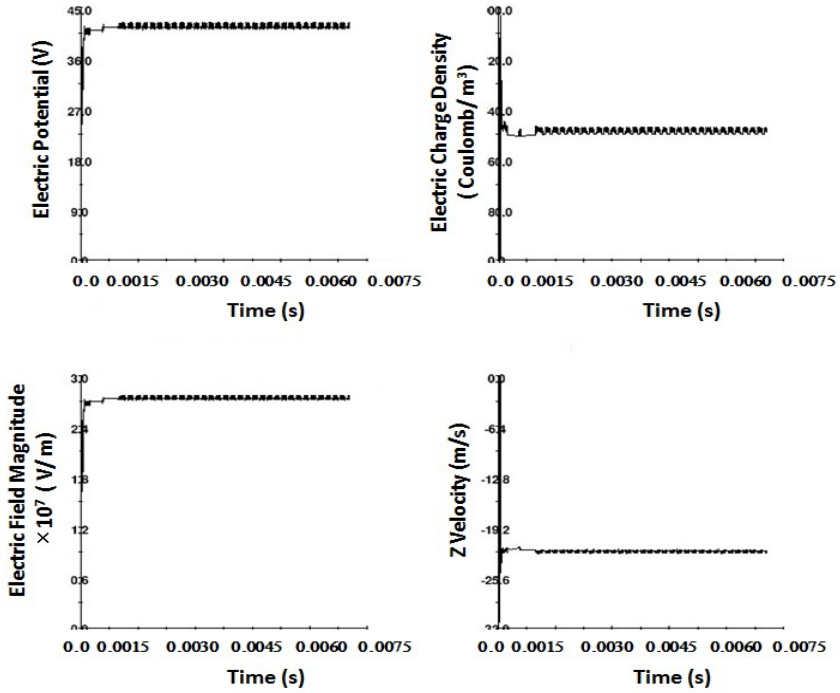

Figure 5.11 The evolution of electric potential (top left), electric charge density (top right), electric field magnitude (bottom left), and axial velocity probed some distance along Z between the emitter and the endplate.

The results of the cylindrical mesh convergence study are shown in Figure 5.12. The jet diameter was probed at the point where the jet reaches the endplate. If the mesh is too coarse, the jet is too thick but a good convergence of the jet diameter was observed below a cell size of 2.5 $\times 10^{-7}$ m. A comparison between the respective computational efforts required is depicted by measuring the CPU time for the first time step (1 microsecond) shown in Figure 5.13. As the cell size decreases, both the computational time and the total number of mesh points increase dramatically. Figure 5.14 shows the relationship between CPU time versus total number of mesh

points. Taking into consideration both the accuracy of the computation and also the computational efficiency, a mesh size of roughly 2.5×10^{-7} m was chosen as a good compromise between accuracy and computational efficiency.

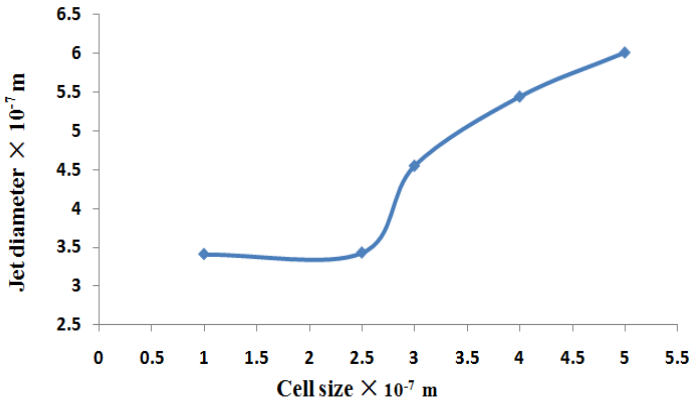

Figure 5.12 Averaged jet diameter plotted versus mesh resolution when jet reaches the outflow boundary.

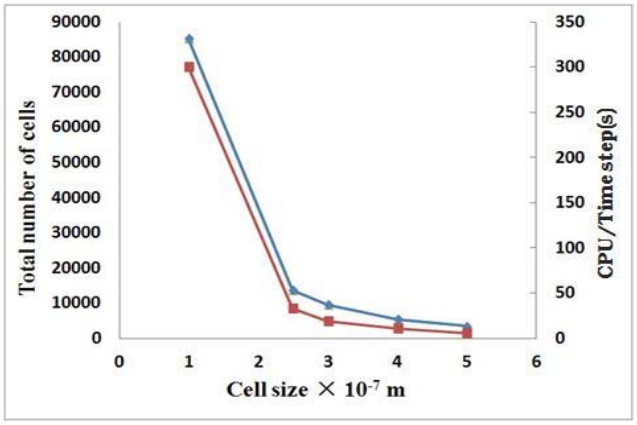

Figure 5.13 Relationship between total number of cells (blue line), CPU time of the first time step (red line), and the computational cell size of the 2D cylindrical mesh.

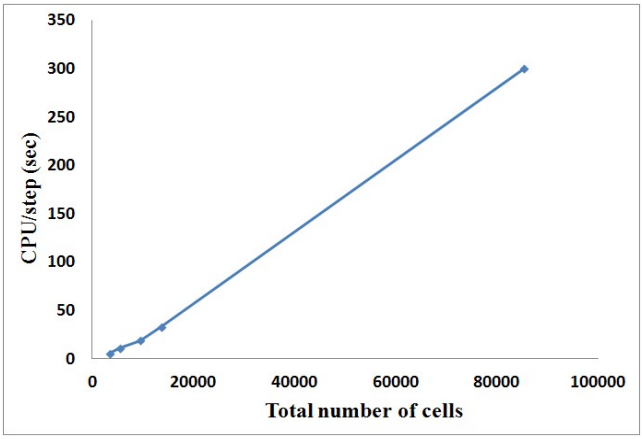

Figure 5.14 CPU time taken within the first calculation time step (1×10^{-6} sec) versus corresponding Total number of cells.

5.2.2 Characterization within Nanoflow Regime

Figure 5.15 shows an astable electrospray mode which might be ascribed as dripping or pulsating mode simulated under the electric potential of 100V and the velocity of 0.02 m/s. Since the electric potential applied was too low under the current inflow velocity, there was not enough force to transport the fluid away and the cone adopted a round shape and deformed towards the counter electrode. Droplets or jets would burst out during the process to decrease the surface energy of the growing cone. Every 'burst-out' would end up with the cone back to its original shape and then it starts to grow again. Figure 5.16 shows just the opposite phenomenon where the applied potential is too high for the velocity used. A small cone was formed because there was not enough support of fluid under this high potential. The jet is too thin and frequently breaks up into sections.

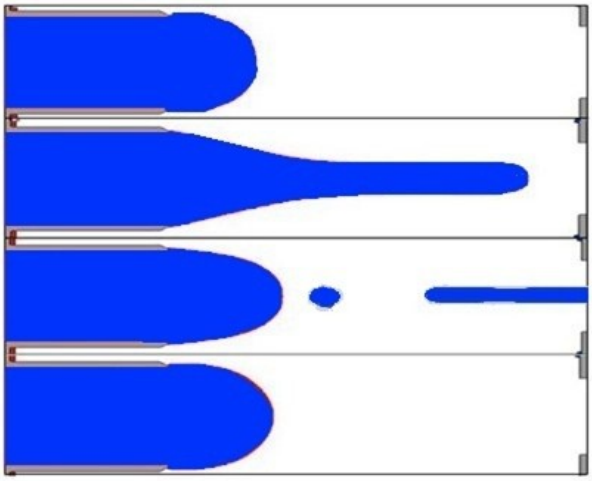

Figure 5.15 Electrospray of various time steps (0.00022s, 0.0005s, 0.00056s, 0.00006s) under the electric potential of 100V and the velocity of 0.02 m/s indicates an astable cone-jet mode where insufficient electric potential was used under the applied inflow rate.

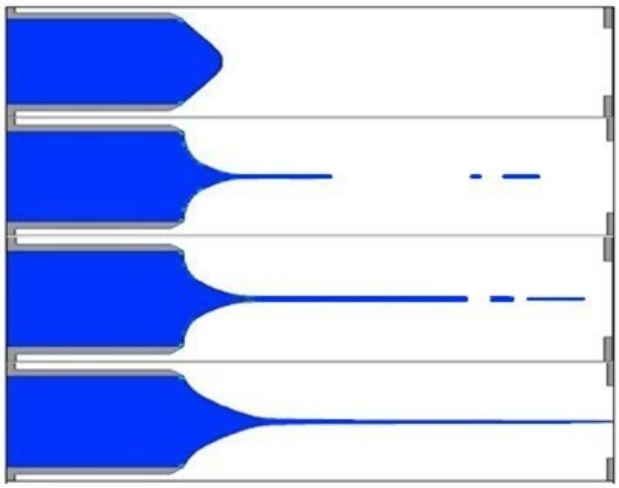

Figure 5.16 Electrospray at various times (0.0002s, 0.00038s, 0.00042s, 0.0007s) indicating an astable cone-jet mode where too high an electric potential 1600V was used under the inflow velocity of 0.04m/s.

The electrospray was examined for a broad range of applied voltage and flow rate to indentify the stable cone-jet region. Operational parameters that are able to generate the cone-jet

state in the simulation are indicated by the shaded region of Figure 5.17. However, this region also includes some astable states of electrospray. In those states, the cone is either too small or elongated to be consistent with the shape Taylor predicted, and the jet keeps growing and shrinking at a certain frequency. The strict determination for the stable cone-jet mode requires also the ion current investigation.

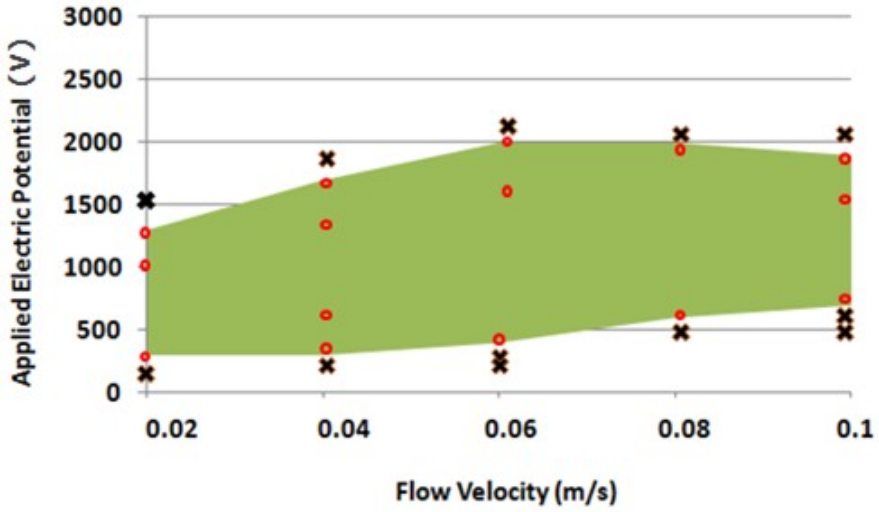

Figure 5.17 Characterization of cone-jet regime (shaded area) for the tapered micro-scale emitter described in Chapter 5.2. Circles represent the simulation trials that are successful in forming the cone-jet, crosses represents the simulation trials that fail to form the cone-jet.

Spray currents under the same inflow velocity of 0.06 m/s, with systematically varied potential difference are plotted in Figure 5.18. The current depicts a linear increase at first but becomes stable under the electric potential between 700 V and 1000 V. The region is assumed to be the stable cone-jet regime. A further increase in the electric potential results in a significant increase in spray current while the jet is seen to be too thin to maintain and breaks up from time

to time. The phenomena observed are very similar to the experimental observations of Smith *et al.*[38] for nano-ESI.

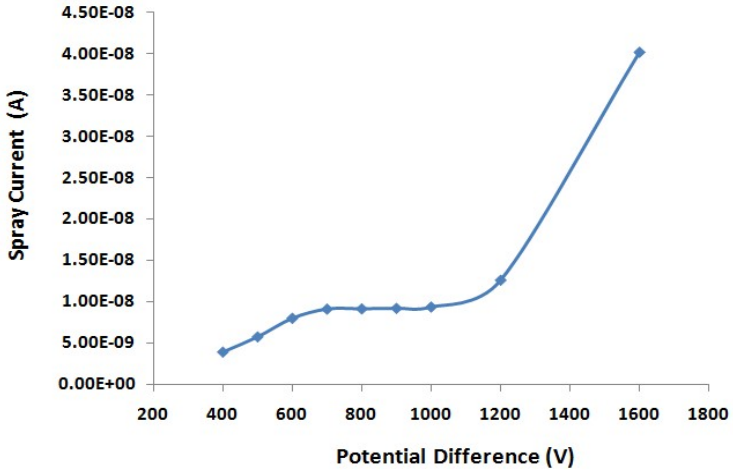

Figure 5.18 Spray current computed with increasing applied electric potential at a constant inflow velocity of 0.06 m/s.

5.2.3 Discrepancy from the Experimental Results

The computational results for the spray current are much lower than the experimental measurements. There are many factors that are responsible for the discrepancy and prevent the direct quantitative comparison between the two.

The first thing is the wetting. In these simulations, a predefined contact angle was not used since it involves a very complex interplay of many physical factors and was found to have a significant impact on the spray characteristics. Second, the tapered emitter tip restricts the Taylor cone base to the i.d. of the emitter channel, i.e. 20 μm. However, in the experiment, wetting expands the Taylor cone base to the outer periphery of the emitter, which actually makes the cone

base roughly 50 μm in diameter. Due to this, the radii of the jets generated in experiments are expected to be larger than those from the simulations. Since the spray current is directly proportional to the radius of the jet, a difference in jet diameter would reasonably affect the final spray current as well.

Finally, any change in any solution properties for spraying like surface tension, dielectric constant, or conductivity would result in a change of ESI behavior and would influence the spray current. The chosen liquid properties for the simulation are from Sen *et al* [55] where the solvent mixture of 50% water and 50% methanol with 1% acetic acid contained was used for their simulation and experiments. However, a difference would reasonably exist from the real solution used in my experiments.

5.2.4 Cartesian Mesh Sensitivity Test – from 2D to 3D

As a preparation for later multi-nozzle electrospray, where a cylindrical mesh is not appropriate, a mesh sensitivity test on the same model was performed for a 3D Cartesian mesh. Here, the flow region is subdivided into a mesh of fixed rectangular cells. Inside each cell, local average values of all physical variables are computed and stored. Velocities are located at cell faces and other variables are located at the centers of the cells. Curved obstacles, wall boundaries, and other geometric features are embedded in the mesh by defining the fractional face areas and fractional volumes of the cells that are open to flow (the *FAVOR*^{TM} method) [92].

The mesh sensitivity test was performed with one quarter of the simulated system

represented with a Cartesian mesh (see Figure 5.19(B)) considering the symmetric feature of the system. A uniform mesh with a mesh size at least 5×10^{-7} m was used in order to resolve the curvature of the emitter end. An X-Z view for the mesh is shown in Figure 5.19(A) and the model preview for the construction (grey) with fluid (blue) resolved is shown in Figure 5.19(C).

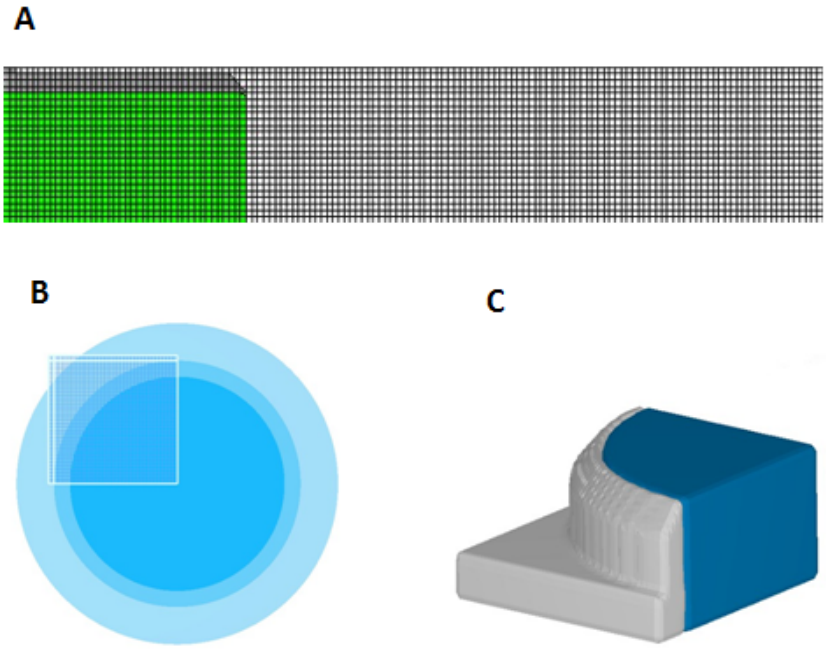

Figure 5.19 (A) Mesh resolution view from X-Z plane of the computational region. (B) Base of the emitter model built shows one quarter of the area covered with Cartesian mesh. (C) Model preview under the applied mesh resolution.

With computational region changes from 2D cylindrical to 3D Cartesian, the number of the mesh increases significantly for the same mesh size (see Table 5.1). As a result, the CPU time for a Cartesian mesh is considerably longer.

Table 5.1 Comparison of computational effort on the same model between cylindrical mesh and Cartesian mesh.

Cell size × 10^{-7} m	**Total number of cells (Cylindrical)**	**Total number of cells (Cartesian)**
5	3408	81792
4	5340	160200
3	9480	379200
2.5	13632	654336
1	85200	8064000

With a 3D Cartesian mesh, not only is much more computational effort required, but also the computational complexity increases. All equations are expanded into three directions and the convergence of computations becomes more challenging within the micro-scale system. Small numerical errors can lead to the collapse of the whole computation and thus should be strictly eliminated. The most common numerical error results from a charged mist or droplet appearing during the formation of the cone-jet region. The existence of these mists or droplets greatly impacts the electric field uniformity and disturbs the computational stability. To avoid the presence of scattered liquids appearing within the computational region, the solid end plate was removed and the peripheral boundary conditions were changed from symmetric to outflow boundary condition.

These measures proved to be rather effective in allowing scattered droplets out once they hit the boundary or the counter end, held at ground potential. 2D and 3D illustrations of the boundary conditions within the computational region are shown in Figure 5.20. The inner two planes of the cone-jet region were set to be symmetric and the outer planes were outflow

boundaries. The end plate boundary was still continuative boundary condition similar to what was used in 2D cylindrical mesh while further imposed of a ground electric potential boundary there. Outflow boundary condition is similar to continuative boundary condition, except that it forces the second derivative of all physical parameters to be zero instead of the first derivative. Thus it is less aggressive and allows the acceleration of the liquid across the boundary plane. It is also applicable to the situation where significant wetting effect exists. Liquid will freely flow out and spread even if it reaches the boundary. The meaning of all other boundary conditions used for the model can be found in Chapter 3.

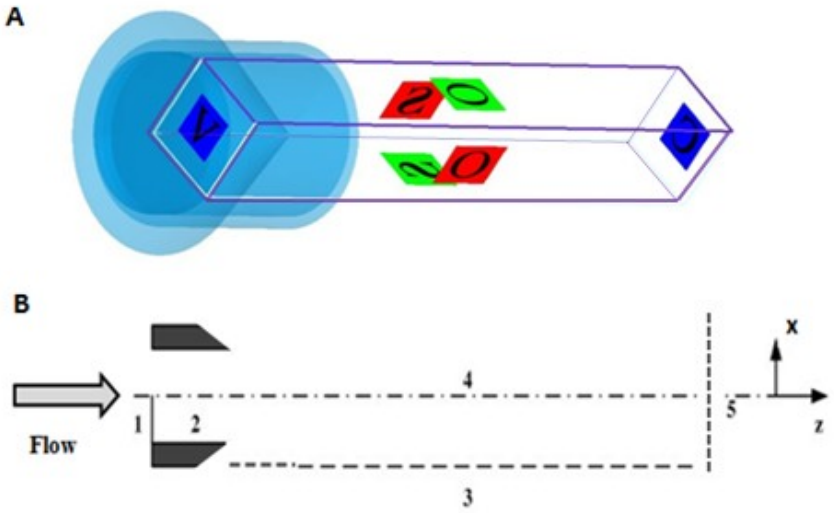

Figure 5.20 (A) 3D computational region with boundary conditions indicated: V-velocity boundary, S-symmetric boundary, O-outflow boundary, C-continuative boundary. (B) 2D (X-Z plane) illustration of boundary conditions: 1-Velocity boundary condition, 2-No slip boundary for the inner wall of the capillary, 3-Outflow boundary condition, 4-Symmetric boundary, 5- Continuative boundary.

As an illustration, a successful generation of a Taylor cone-jet with Cartesian mesh is shown in Figure 5.21. Only one quarter of the system was computed and displayed, and the result

is plotted with electric charge density contours. The charges are exclusively accumulated on the liquid surface as expected and gradually transported towards the counter electrode along the jet. The simulation process and features calculated by Cartesian mesh are very similar to those from the cylindrical mesh and the electric charge density is seen to be mostly accumulated on the surface of the cone-base and jet.

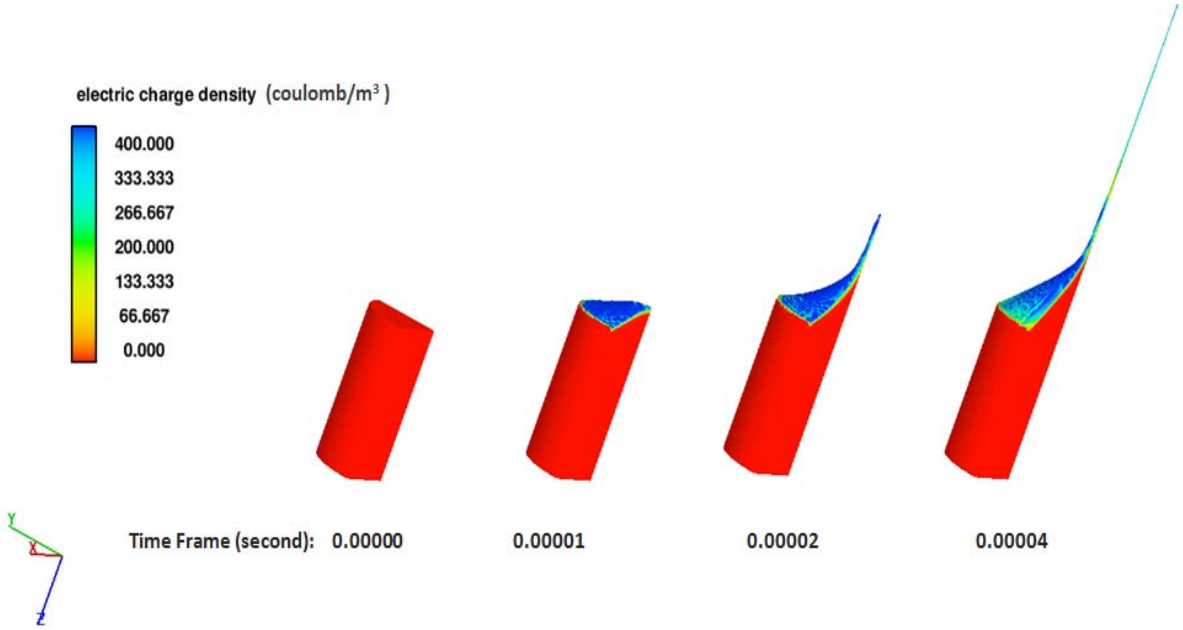

Figure 5.21 Generation of a Taylor-cone jet process at different time frames under the electric potential 800V and inflow velocity 0.09m/s plotted together with electric charge density contours.

The results from the convergence test were shown in Figure 5.22. The jet radius gradually converges below the cell size of 3×10^{-7} m. CPU time required for different levels of computational mesh is indicated in Figure 5.23. The optimal mesh size is thus around 2.5×10^{-7} m where reasonable computational efficiency and accuracy were achieved. This value will be a

good reference for future simulations on multi-nozzle emitters using Cartesian mesh. Note that the CPU time per time step in Figure 5.23 is much larger than for a cylindrical mesh (see Figure 5.15).

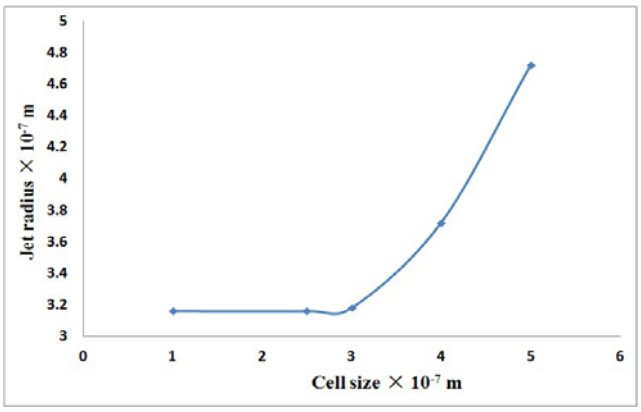

Figure 5.22 Averaged jet diameter plotted versus mesh resolution when jet reaches the outflow boundary using Cartesian mesh.

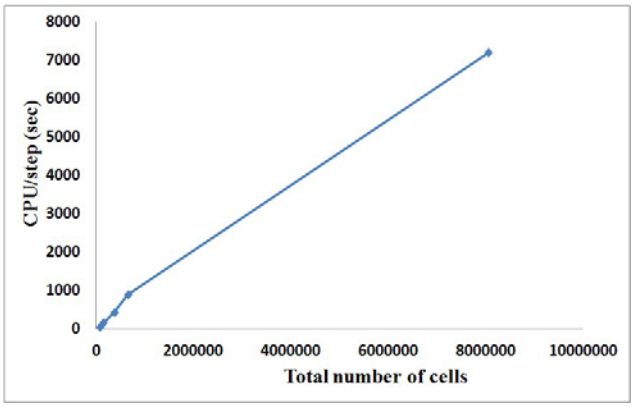

Figure 5.23 CPU time taken within the first calculation time step (1e-6 sec) versus corresponding Total number of cells using Cartesian mesh.

5.3 Nano-ESI Simulation with 2-hole Emitter

5.3.1 Description of Computational Model

A schematic diagram of the 2-hole emitter based ESI model for simulation is shown in Figure 5.24. The 2-hole emitter model comprises two identical nozzles for spraying with each nozzle being 20 μm i.d. and placed 180 μm apart (from centre to centre). Starting with a relatively large distance between the nozzles that was expected to provide individual sprays, the separation between the emitter and the counter electrode plate is kept at 0.2 mm. A potential difference 2 kV has been applied and maintained between the emitter and the counter electrode. The liquid sample for spraying is the same as the one used for nano-ESI 1-hole emitter simulation.

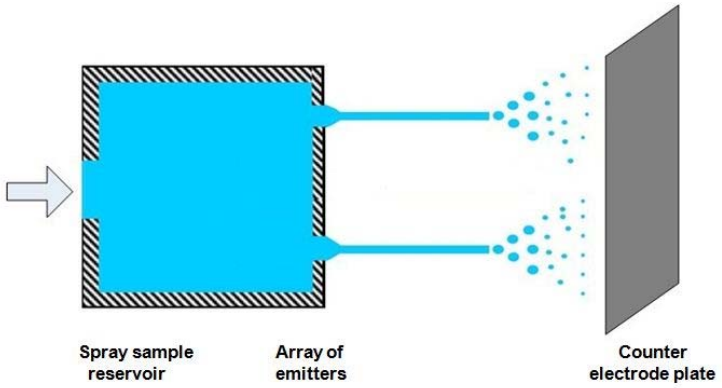

Figure 5.24 Illustration of a typical 2-hole emitter multi-electrospray experiment.

5.3.2 Mesh and Boundary Conditions

Taking advantage of the symmetric feature of the 2-hole emitter, only the upper half of the system was covered by computational mesh for simulation. A non-uniform 3-D computational

mesh was built around the model with (120, 22, 110) cells in (x,y,z) directions. Figure 5.25 (A) and (B) show respectively the x-y and x-z view of the mesh. A finer mesh was applied in the expected cone-jet region from each nozzle. Figure 5.25 (C) is the preview for the construction resolved under the current mesh applied.

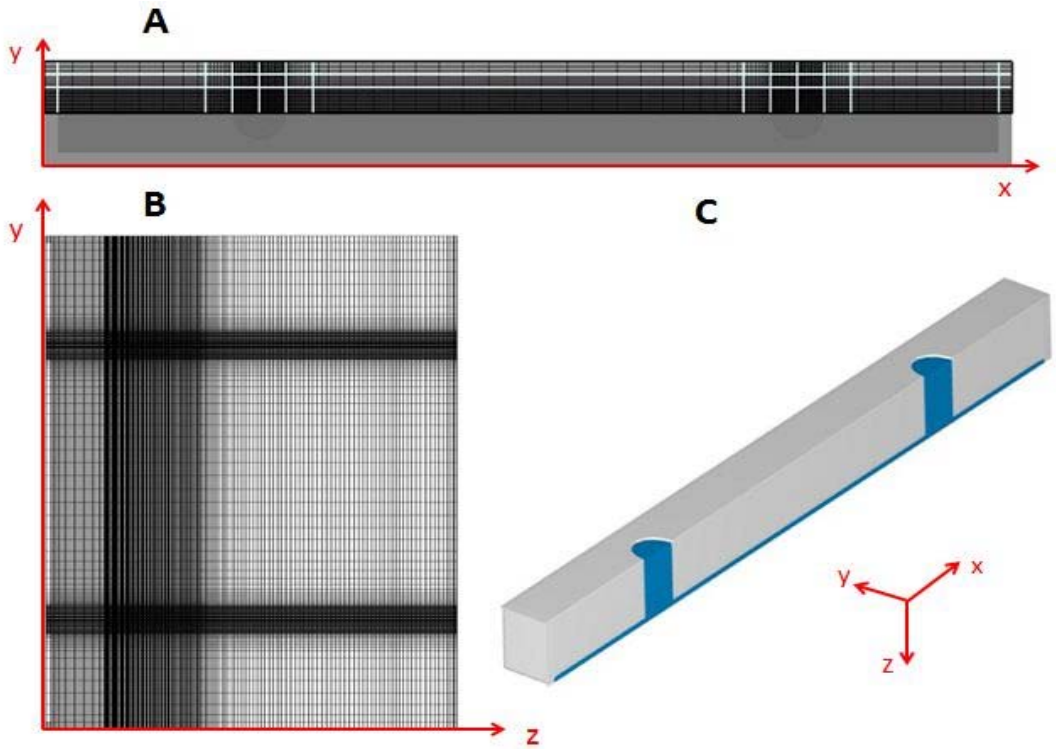

Figure 5.25 (A) Non-uniform 3D mesh in (x, y) plane; (B) Non-uniform 3-D mesh in (x, z) plane; (C) Preview of the construction resolved under the current mesh.

The boundary conditions for the 2-hole ESI model are illustrated in Figure 5.26. A velocity boundary condition was set at a constant velocity for inflow liquid acting like a pump. Continuative boundary conditions were set at the outflow boundary plate with a zero electric potential assigned. The plane which separates the upper and lower part of the system is set to be a

symmetric boundary. All other computational planes were set as outflow boundary condition so that droplets and mists could freely go out of the computational region.

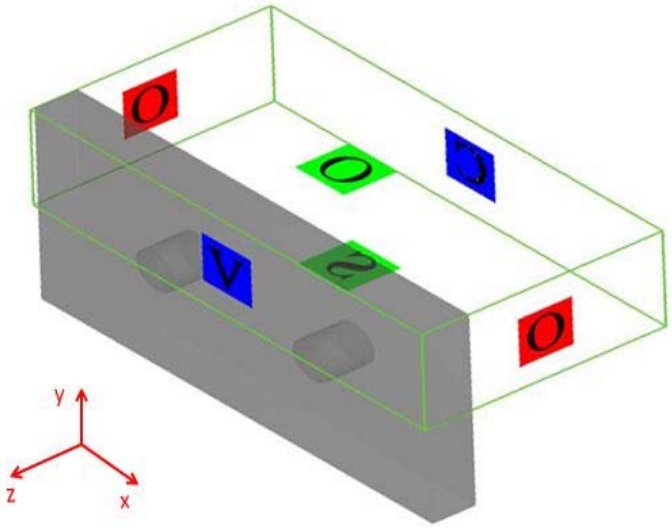

Figure 5.26 Boundaries of the computational domain for the 2-hole electrospray model.

5.3.3 Results and Discussion

The profiles of the two electrosprays are shown in Figure 5.27 plotted together with electric potential contours. Multi-spray was successfully generated and two jets appear to be semi-parallel to each other. The current MES model was simulated with the inflow velocity 0.09 m/s and a potential difference of 2000 V. The initial onset potential was found to be several hundreds of volts higher than the previous single-emitter case under the same inflow velocity. This is mainly due to the fact that the single-hole emitter tip has a sharp tapered shape which induces a higher local electric field than a flat tip. Despite the large distance (180 μm) between the two nozzles (centre to centre), the completely independent two Taylor cone-jets were not reached. Though

telling from Figure 5.27, the electric field lines were not influenced between two charged Taylor cone-jets, the base of the Taylor cones are seen to be slightly deformed. A repulsive force pushes one cone-jet away from the other.

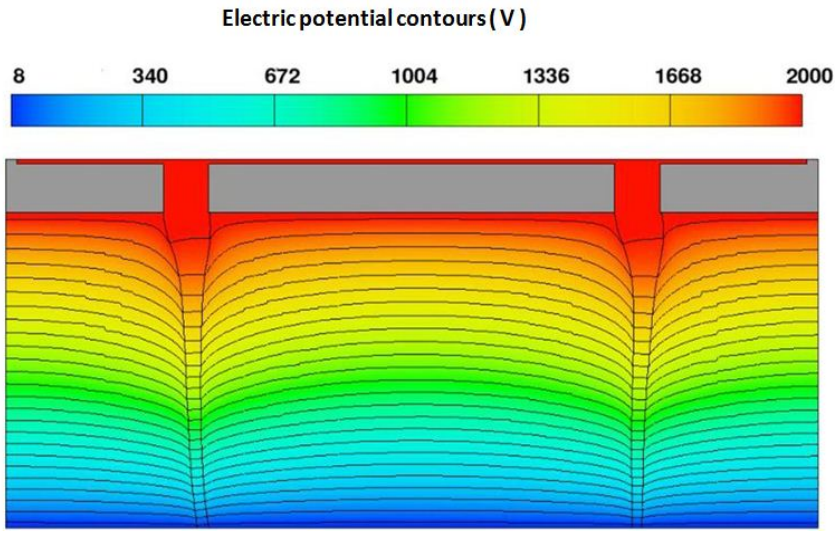

Figure 5.27 2D profile of a two-hole electrospray where relatively independent cone-jets are formed under the electric potential of 2kV and inflow velocity of 0.09 m/s.

To investigate the influence of the distance between holes on multi-electrospray performance, similar simulations were performed under the same physical condition while the distance between the two holes was only 60 μm (from centre to centre). As expected, the simulation result shows a strong repulsion between two cone-jets since they are both positively charged on the surface (see Figure 5.28(left)). Figure 5.28 shows only an instantaneous snapshot during the electrospray process and thus the two jets are not identical. If sufficiently long computations are run, the average jet position would be the same for both channels. A similar

phenomenon was observed in ESI experimental observation on the right that was specifically described in Chapter 4. Also, in both simulation and the experiments, the applied voltage was found to be much higher than the regular single-aperture ESI in order to achieve multi-spray.

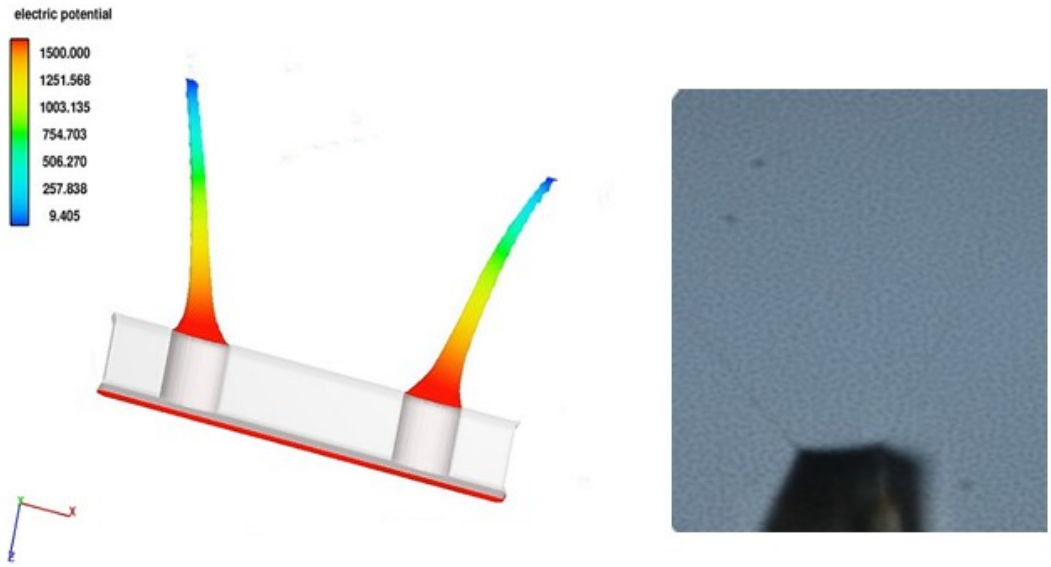

Figure 5.28 3D plot of a two nozzle electrospray in simulation (left) shows a significant repulsion between two charged jets and (right) similar experimental observation in 2-hole emitter ESI.

Paralleled simulations were further performed under varied electric potential while keeping all other physical parameters exactly the same (Figure 5.29). With increased electric potential, the jets become thinner and the repelling becomes more and more significant. When the electric potential was as high as 2000V, the base of the Taylor cone was seen to move outwards and gradually deviate from the original channel. This was due to an increased surface charge under a higher applied potential.

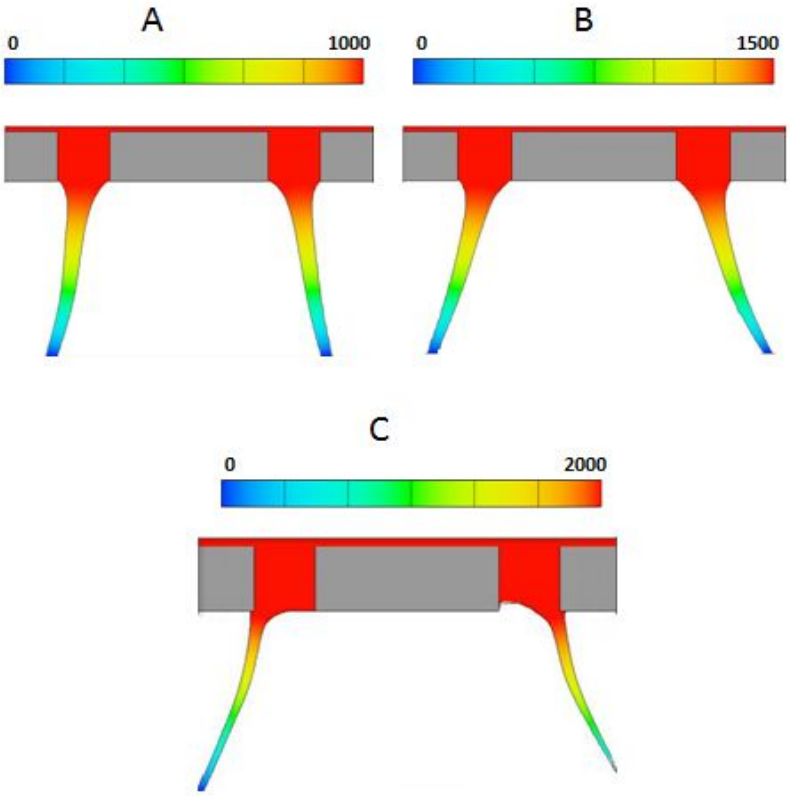

Figure 5.29 Effect of electric potential on multi-electrospray performance at the same velocity of 0.09m/s under various applied electric potential (Applied electric potential from A to C : 1000V, 1500V, 2000V respectively).

5.4 Nano-ESI Simulation with 3-hole Emitter

The computational model for simulating multi-spray with 3-hole emitter is similar to the 2-hole case, only the emitter was different. The current 3-hole emitter was built with each channel 20 μm i.d. and was positioned at the three vertices of an equilateral triangle. The edge length for the triangle (from hole centre to centre) was 180 μm (same as the distance for 2-hole emitter model to achieve MES). All the boundary conditions are the same as those applied on 2-hole emitter ESI model. A non-uniform Cartesian mesh was applied with finer mesh built around three hole region

and was (160,112,130) in (x,y,z) direction. The x-y plane of the mesh resolution is shown in Figure 5.30.

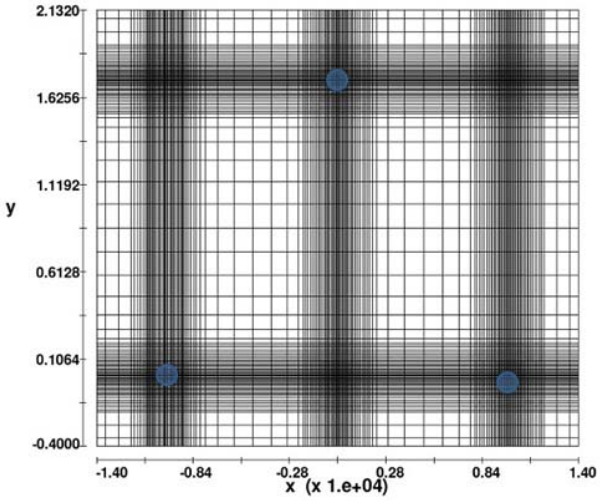

Figure 5.30 Non-uniform 3D mesh in (x, y) plane applied on 3-hole emitter.

In Figure 5.31, the successful generation of multi-electrospray with a 3-hole emitter is presented. Current multi-electrospray was simulated at a constant velocity of 0.02 m/s at the inflow boundary plane with an applied potential of 2 kV. Though independent cone-jets have formed, the interference among the three charged jets is clearly seen. Qualitative comparisons with the experimental observation from different views are shown in Figure 5.32. Figure 5.32(A) is the x-y plane viewed from Z min to Z max simulated cone-jet. Instead of pointing straight forward to the counter ground, three jets all repel one another and diverge. The phenomenon is rather similar to the experiments shown on the right. Figure 5.32(B) shows the similar repulsion from the side view.

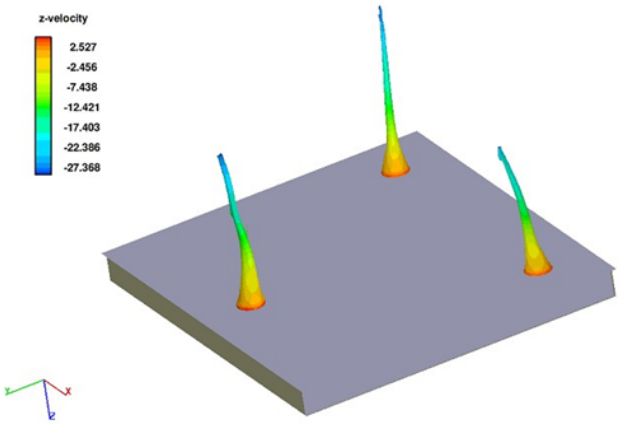

Figure 5.31 Simulated Multi-ESI with a 3-hole emitter under inflow velocity of 0.02 m/s and the applied potential of 2kV.

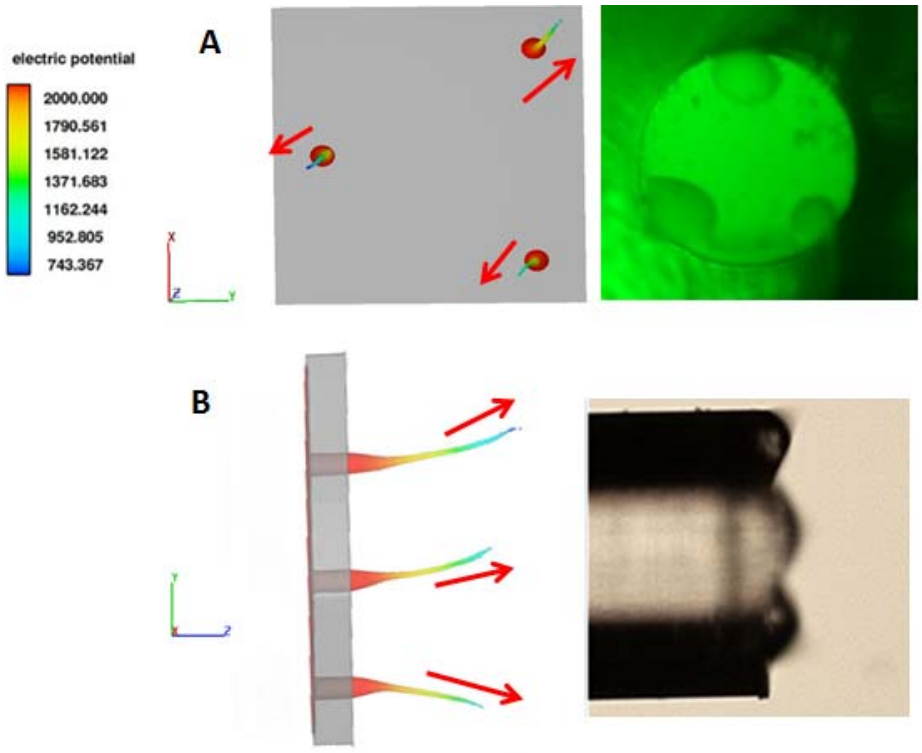

Figure 5.32 Comparison of multiple electrospray with 3-aperture emitter showing similar repelling force between charged jets. (A) A look down view on x-y plane. (B) A side view on y-z plane.

5.5 Summary

The dynamic physical phenomenon of electrospray has been successfully simulated. A validation test was first performed with a macro-scale 1-hole emitter. The transient cone-jet formation was fully investigated qualitatively and the characteristic curve for spray current under various parameters was quantitatively studied under steady state. The simulation results show good agreement with previous experimental studies.

Further simulation for electrospray was performed with an emitter under micro-scale conditions. The investigation for cone-jet formation is quite similar to my experimental observation (Chapter 4) and CFD simulations were proved to be able to capture several interesting astable states of electrospray. Simulation predictions for spray current under different parameters share the same trend as the characterization curve obtained from the experimental measurements. A better numerical scheme for electrospray under micro-scale was reached from mesh sensitivity test. The relationship between CPU time and mesh scale was investigated and the optimal mesh size for both cylindrical mesh and Cartesian mesh was found.

Multi-electrospray was successfully simulated with a 2-hole and 3-hole emitter model. In the former case, two relatively independent cone-jets were formed with a large distance between holes. A significant repulsion between charged jets was captured when two holes are closer to each other, conforming to the experimental observation. Moreover, the effect of applied potential on the two cone-jets was further studied and the results indicate a greater repulsive force under a

higher electric field. For the 3-hole emitter model, the similar repulsion was observed among three charged cone-jets. It seems that in order to achieve the true independent spray, the distance has to be even further away between holes (at least more than 180 μm from centre to centre).

Chapter 6 Conclusion and Outlook

6.1 Conclusion

This thesis presents a joint project of both numerical simulation and analytical experiments on electrospray with various types of emitters. It was developed from the idea of a cost-effective and efficient numerical tool for testing electrospray performance with various emitter designs. Few papers could be referred to in terms of simulating the whole dynamic process of this interesting physical phenomenon and it is a rather novel and challenging field. The lack of previous work likely stems from several factors. First, electrohydrodynamic flow equations are complex and difficult to solve. Few computational packages can treat these flows. Second, the computational tools are primarily intended for engineering applications. Chemists have little familiarity with the tools and the background required for these simulations.

In this work, a commercial CFD code based on Melcher & Taylor's Leaky-dielectric model was employed to simulate the transient physical process of electrospray. The methodology of using CFD simulation as the main approach in this work has proved to have the unique capability of describing the full dimensionality of the cone-jet formation. With detailed information obtained for physical properties, we are able to trace and further investigate the physical process at a deeper level. The simulation results were compared with laboratory experiments both qualitatively and quantitatively. The benchmarking result on the successful simulation of a micro-scale emitter achieved in this work is believed to be the smallest scale of the dynamic simulation

case for electrospray published in the literature to date. As a summary, the following lists some of the main achievements in this project.

- **Single electrospray with a R= 350 μm emitter**

Starting with the validation test on a macro-scale 1-hole model, a detailed characterization for the physical phenomenon of electrospray was described. Consecutive stages during cone-jet formation were visually demonstrated with electric field contours; the velocity profile in the steady state as well as the electric charge distribution within liquid region was also presented. The information clearly uncovers different aspects of the physical nature of electrospray. Spray current along the jet was further calculated and averaged within time and space. The prediction for the change of spray current under various applied potential and flow rates are in extensive agreement with previous experimental observations in literatures[38, 40, 91]. Further simulations were performed to test the effect of various parameters on final electrospray performance like the emitter tip property, flow rate.

- **Single electrospray with a R = 10 μm emitter**

Following the validation test, a real world prototype of a 20 μm i.d. emitter model was built and its electrospray process was successfully simulated. Similar to the experimental observations (see Chapter 3.1), this tapered single-hole emitter could be operated in a stable cone-jet mode under a wide range of electric potentials and flow rates. The tapered design at the tip of the emitter helps the electrospray to stabilize at the base of the Taylor cone. The characterization curve for spray

current change with the increased applied potential is consistent with previous studies [38] as well as my experimental measurements. It is also exciting to find that the simulation is able to capture some of the astable modes of electrospray clearly and helps us to distinguish between different electrospray modes and find the optimal conditions under which the cone-jet mode occurs.

- **Multi-electrospray with 2-hole and 3-hole emitter**

Based on the 10 μm emitter model, a multi-electrospray was successfully generated with a 2-hole and 3-hole emitter. Comparative simulations performed on 2-hole emitter electrospray shows that the distance between the nozzles plays a very important role in electrospray performance. If the two-holes are not separated enough, the two charged jets repel each other, which could not provide the ideal spray results for ESI-MS applications. Moreover, the repulsive effect is found to become more significant with the increasing electric potential. The relatively independent electrospray was stabilized for 2-hole emitter spray where holes are at a distance of 180 μm (from centre to centre) away. However, for 3-hole emitter spray, the same distance doesn't seem to be enough to provide independent jets. Three charged cone-jets were observed to be pointing against one another.

6.2 Future Work and Recommendations

Taking advantage of CFD tools to test the effect of different emitter designs on electrospray performance in this work marks only the first steps in this direction. Clearly, the topic is rich with so many things waiting to be done.

The trials in my project currently only touch the qualitative study for 2-hole and 3-hole emitter model with relatively simple design and pattern of the emitter nozzle. Future work would be extended to the spray current calculation for multi-sprays and the simulation of the electrospray with more complex muti-nozzle emitter designs. These include the variation of the number of nozzles, the size of the nozzle, the distance between channels, the hole pattern, and the shape of the tip *etc*.

A main issue regarding multi-electrospray simulation is the considerably long calculation time. It is largely due to the huge number of the mesh points required. With a relatively awkward single mesh applied, a large area is actually wasted. As an illustration, Figure 6.1 shows a typical mesh for a 6-hole nozzle model. To better refine the areas from which cone-jet would be generated, other places like where the arrows indicate are also represented with a fine mesh. Thus, lots of mesh points are wasted on regions that are less relevant to the physical process of interest. Multi-block techniques are a potential solution to address the problem. For example, nested blocks could be applied for sparse holes. Since the ratio of mesh size difference should not go above 1:2 to maintain the numerical accuracy, several layers of nested meshes would be required within each nozzle. Another possible way is to link several mesh blocks for the computational region: fine mesh block for each hole and coarse mesh block for area of less interest. Careful attention should be paid on the boundary where blocks are linked and it is better to avoid a sharp change in mesh size across the boundary from block to block. It is anticipated that much time and effort would be devoted first to find an optimal mesh pattern for simulating multi-hole emitter

electrospray. And once the mesh is settled for one case, it would be much easier to be applied to other multi-spray simulations.

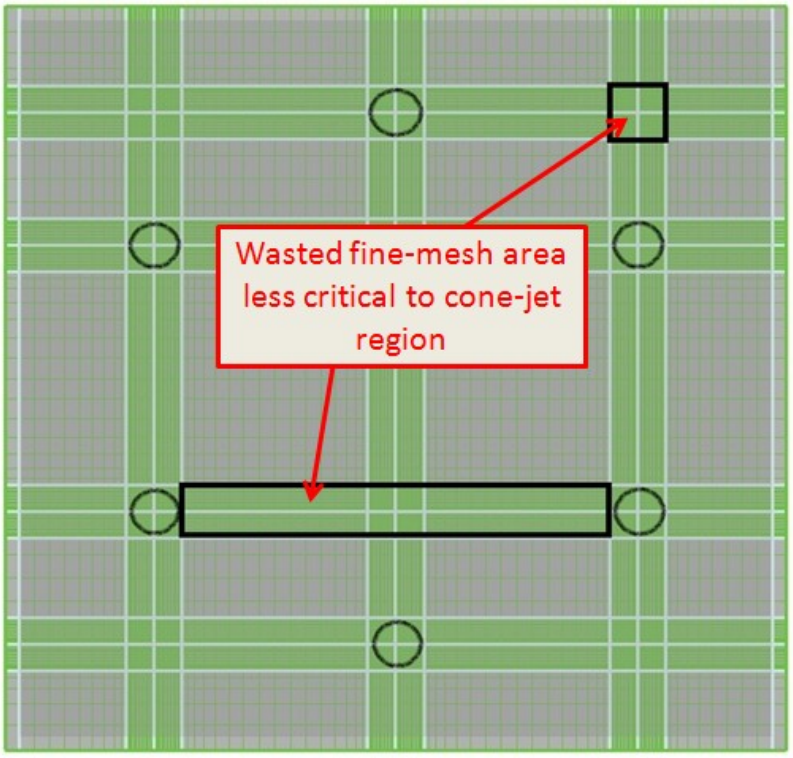

Figure 6.1 Illustration of a typical 6-hole emitter model with non-uniform mesh applied.

From the beginning of this work, we have hoped to build a visual lab as close to real experimental condition as possible for an accurate comparison. Still, many compromises have to be made at first to simplify the physical picture to focus on the more important issues. Once the important issues are clear, each of those previously neglected factors itself would indeed be another interesting scientific topic. For example, the relationship between wetting effect on the emitter tip and the final electrospray performance.

As mentioned at the very beginning of the thesis, the jet breakup and droplet formation scenario are beyond the scope of this work. However, this is definitely another valuable direction to follow that could help to explore the complete electrospray phenomenon. To achieve this goal, equations upon which current software is based would need to be modified. It is a challenging job while some of the groundwork for this has already begun. In a newly published paper in 2011, the Sen *et al.* extended their previous work to the simulation of jet breakup in electrospray ionization with a microfluidic emitter [93]. In their work, the existing code based on leaky-dielectric model is modified to allow the presence of free charges inside the bulk fluid. A small velocity perturbation is further introduced at the inflow boundary to imitate the natural disturbance that is necessary for the jet break up. The simulation prediction was reported to be in good agreement with experiments.

Bibliography

1. Mclafferty, F.W., *Tandem Fourier-Transform Mass-Spectrometry of Large Molecules.* Abstracts of Papers of the American Chemical Society, 1986. **192**: p. 21-Anyl.
2. Griffiths, W.J. and Y.Q. Wang, *Mass spectrometry: from proteomics to metabolomics and lipidomics.* Chemical Society Reviews, 2009. **38**(7): p. 1882-1896.
3. Gibson, G.T.T., S.M. Mugo, and R.D. Oleschuk, *Nanoelectrospray Emitters: Trends and Perspective.* Mass Spectrometry Reviews, 2009. **28**(6): p. 918-936.
4. Cech, N.B. and C.G. Enke, *Practical implications of some recent studies in electrospray ionization fundamentals.* Mass Spectrometry Reviews, 2001. **20**(6): p. 362-387.
5. Su, S., *Development and Application of Non-tapered Electrospray Emitters for Nano-ESI Mass Spectrometry*, in *Chemistry*. 2008, Queen's University: Kingston. p. 185.
6. Zeleny, J., *The electrical discharge from liquid points, and a hydrostatic method of measuring the electric intensity at their surfaces.* Physical Review, 1914. **3**(2): p. 69-91.
7. Dole, M., L.L. Mack, and R.L. Hines, *Molecular Beams of Macroions.* Journal of Chemical Physics, 1968. **49**(5): p. 2240-&.
8. Yamashita, M. and J.B. Fenn, *Negative-Ion Production with the Electrospray Ion-Source.* Journal of Physical Chemistry, 1984. **88**(20): p. 4671-4675.
9. Kebarle, P. and U.H. Verkerk, *Electrospray: From Ions in Solution to Ions in the Gas Phase, What We Know Now.* Mass Spectrometry Reviews, 2009. **28**(6): p. 898-917.
10. Taylor, G., *Disintegration of Water Drops in Electric Field.* Proceedings of the Royal Society of London Series a-Mathematical and Physical Sciences, 1964. **280**(138): p. 383.
11. Cole, R.B., *Some tenets pertaining to electrospray ionization mass spectrometry.* Journal of Mass Spectrometry, 2000. **35**(7): p. 763-772.
12. Rayleigh, L., *On the equilibrium of liquid conducting masses charged with electricity.* Philos. Mag., 1882. **14**: p. 184-186.
13. Mack, L.L., et al., *Molecular Beams of Macroions .2.* Journal of Chemical Physics, 1970. **52**(10): p. 4977-&.
14. Gamero-Castano, M. and J.F. de la Mora, *Kinetics of small ion evaporation from the charge and mass distribution of multiply charged clusters in electrosprays.* Journal of Mass Spectrometry, 2000. **35**(7): p. 790-803.
15. Gamero-Castano, M. and J.F. de la Mora, *Modulations in the abundance of salt clusters in electrosprays.* Analytical Chemistry, 2000. **72**(7): p. 1426-1429.
16. Loscertales, I.G. and J.F. Delamora, *Experiments on the Kinetics of Field Evaporation of Small Ions from Droplets.* Journal of Chemical Physics, 1995. **103**(12): p. 5041-5060.
17. Rohner, T.C., N. Lion, and H.H. Girault, *Electrochemical and theoretical aspects of electrospray ionisation.* Physical Chemistry Chemical Physics, 2004. **6**(12): p. 3056-3068.

18. Iribarne, J.V. and B.A. Thomson, *Evaporation of Small Ions from Charged Droplets.* Journal of Chemical Physics, 1976. **64**(6): p. 2287-2294.
19. Meng, C.K. and J.B. Fenn, *Formation of Charged Clusters during Electrospray Ionization of Organic Solute Species.* Organic Mass Spectrometry, 1991. **26**(6): p. 542-549.
20. Nohmi, T. and J.B. Fenn, *Electrospray Mass-Spectrometry of Poly(Ethylene Glycols) with Molecular-Weights up to 5 Million.* Journal of the American Chemical Society, 1992. **114**(9): p. 3241-3246.
21. de la Mora, J.F., *Electrospray ionization of large multiply charged species proceeds via Dole's charged residue mechanism.* Analytica Chimica Acta, 2000. **406**(1): p. 93-104.
22. Iavarone, A.T., J.C. Jurchen, and E.R. Williams, *Supercharged protein and peptide lone formed by electrospray ionization.* Analytical Chemistry, 2001. **73**(7): p. 1455-1460.
23. Hogan, C.J., et al., *Charge carrier field emission determines the number of charges on native state proteins in electrospray ionization.* Journal of the American Chemical Society, 2008. **130**(22): p. 6926-+.
24. Nguyen, S. and J.B. Fenn, *Gas-phase ions of solute species from charged droplets of solutions.* Proceedings of the National Academy of Sciences of the United States of America, 2007. **104**(4): p. 1111-1117.
25. Luedtke, W.D., et al., *Nanojets, electrospray, and ion field evaporation: Molecular dynamics simulations and laboratory experiments.* Journal of Physical Chemistry A, 2008. **112**(40): p. 9628-9649.
26. Enke, C.G., *A predictive model for matrix and analyte effects in electrospray ionization of singly-charged ionic analytes.* Analytical Chemistry, 1997. **69**(23): p. 4885-4893.
27. Maze, J.T., T.C. Jones, and M.F. Jarrold, *Negative droplets from positive electrospray.* Journal of Physical Chemistry A, 2006. **110**(46): p. 12607-12612.
28. Kebarle, P. and M. Peschke, *On the mechanisms by which the charged droplets produced by electrospray lead to gas phase ions.* Analytica Chimica Acta, 2000. **406**(1): p. 11-35.
29. Loeb, L.B., A.F. Kip, and G.G. Hudson, *Pulses in negative point-to-plane corona.* Physical Review, 1941. **60**(10): p. 714-722.
30. Cole, R.B., *Electrospray ionization mass spectrometry : fundamentals, instrumentation, and applications*. 1997, New York: Wiley. xix, 577 p.
31. Smith, D.P.H., *The Electrohydrodynamic Atomization of Liquids.* Ieee Transactions on Industry Applications, 1986. **22**(3): p. 527-535.
32. Taylor, G.I. and A.D. Mcewan, *Stability of a Horizontal Fluid Interface in a Vertical Electric Field.* Journal of Fluid Mechanics, 1965. **22**: p. 1-&.
33. Ikonomou, M.G., A.T. Blades, and P. Kebarle, *Electrospray Mass-Spectrometry of Methanol and Water Solutions Suppression of Electric-Discharge with Sf6 Gas.* Journal of the American Society for Mass Spectrometry, 1991. **2**(6): p. 497-505.

34. Wampler, F.M., A.T. Blades, and P. Kebarle, *Negative-Ion Electrospray Mass-Spectrometry of Nucleotides - Ionization from Water Solution with Sf6 Discharge Suppression.* Journal of the American Society for Mass Spectrometry, 1993. **4**(4): p. 289-295.
35. Marginean, I., P. Nemes, and A. Vertes, *Order-chaos-order transitions in electrosprays: The electrified dripping faucet.* Physical Review Letters, 2006. **97**(6): p. -.
36. Marginean, I., P. Nemes, and A. Vertes, *Astable regime in electrosprays.* Physical Review E, 2007. **76**(2): p. -.
37. Nemes, P., I. Marginean, and A. Vertes, *Spraying mode effect on droplet formation and ion chemistry in electrosprays.* Analytical Chemistry, 2007. **79**(8): p. 3105-3116.
38. Marginean, I., et al., *Electrospray characteristic curves: In pursuit of improved performance in the nanoflow regime.* Analytical Chemistry, 2007. **79**(21): p. 8030-8036.
39. Page, J.S., et al., *Subambient pressure ionization with nanoelectrospray source and interface for improved sensitivity in mass spectrometry.* Analytical Chemistry, 2008. **80**(5): p. 1800-1805.
40. Delamora, J.F. and I.G. Loscertales, *The Current Emitted by Highly Conducting Taylor Cones.* Journal of Fluid Mechanics, 1994. **260**: p. 155-184.
41. Ganan-Calvo, A.M., *On the general scaling theory for electrospraying.* Journal of Fluid Mechanics, 2004. **507**: p. 203-212.
42. Smith, D.R., G. Sagerman, and T.D. Wood, *Design and development of an interchangeable nanomicroelectrospray source for a quadrupole mass spectrometer.* Review of Scientific Instruments, 2003. **74**(10): p. 4474-4477.
43. Barnidge, D.R., S. Nilsson, and K.E. Markides, *A design for low-flow sheathless electrospray emitters.* Analytical Chemistry, 1999. **71**(19): p. 4115-4118.
44. Guzzetta, A.W., R.A. Thakur, and I.C. Mylchreest, *A robust micro-electrospray ionization technique for high-throughput liquid chromatography/mass spectrometry proteomics using a sanded metal needle as an emitter.* Rapid Communications in Mass Spectrometry, 2002. **16**(21): p. 2067-2072.
45. Wilm, M. and M. Mann, *Analytical properties of the nanoelectrospray ion source.* Analytical Chemistry, 1996. **68**(1): p. 1-8.
46. Covey, T.R. and D. Pinto, *Practical Spectroscopy*. Vol. 32. 2002.
47. Kelly, R.T., et al., *Nanoelectrospray emitter arrays providing interemitter electric field uniformity.* Analytical Chemistry, 2008. **80**(14): p. 5660-5665.
48. Choi, Y.S. and T.D. Wood, *Polyaniline-coated nanoelectrospray emitters treated with hydrophobic polymers at the tip.* Rapid Communications in Mass Spectrometry, 2007. **21**(13): p. 2101-2108.
49. Tojo, H., *Properties of an electrospray emitter coated with material of low surface energy.* Journal of Chromatography A, 2004. **1056**(1-2): p. 223-228.

50. Liu, J., et al., *Electrospray ionization with a pointed carbon fiber emitter.* Analytical Chemistry, 2004. **76**(13): p. 3599-3606.
51. Sen, A.K., et al., *Modeling and characterization of a carbon fiber emitter for electrospray ionization.* Journal of Micromechanics and Microengineering, 2006. **16**(3): p. 620-630.
52. Tang, K.Q., et al., *Generation of multiple electrosprays using microfabricated emitter arrays for improved mass spectrometric sensitivity.* Analytical Chemistry, 2001. **73**(8): p. 1658-1663.
53. Deng, W. and A. Gomez, *Influence of space charge on the scale-up of multiplexed electrosprays.* Journal of Aerosol Science, 2007. **38**(10): p. 1062-1078.
54. Su, S.Q., et al., *Microstructured Photonic Fibers as Multichannel Electrospray Emitters.* Analytical Chemistry, 2009. **81**(17): p. 7281-7287.
55. Sen, A.K., J. Darabi, and D.R. Knapp, *Simulation and parametric study of a novel multi-spray emitter for ESI-MS applications.* Microfluidics and Nanofluidics, 2007. **3**(3): p. 283-298.
56. Hayati, I., A. Bailey, and T.F. Tadros, *Investigations into the Mechanism of Electrohydrodynamic Spraying of Liquids .2. Mechanism of Stable Jet Formation and Electrical Forces Acting on a Liquid Cone.* Journal of Colloid and Interface Science, 1987. **117**(1): p. 222-230.
57. Glonti, G.A., *On the Theory of the Stability of Liquid Jets in an Electric Field.* Soviet Physics Jetp-Ussr, 1958. **7**(5): p. 917-918.
58. Nayyar, N.K. and G.S. Murty, *The Stability of a Dielectric Liquid Jet in the Presence of a Longitudinal Electric Field.* Proceedings of the Physical Society of London, 1960. **75**(483): p. 369-373.
59. Allan, R.S. and S.G. Mason, *Particle Behaviour in Shear and Electric Fields .1. Deformation and Burst of Fluid Drops.* Proceedings of the Royal Society of London Series a-Mathematical and Physical Sciences, 1962. **267**(1328): p. 45-&.
60. Melcher, J.R. and G.I. Taylor, *Electrohydrodynamics - a Review of Role of Interfacial Shear Stresses.* Annual Review of Fluid Mechanics, 1969. **1**: p. 111-&.
61. Saville, D.A., *Electrohydrodynamics: The Taylor-Melcher leaky dielectric model.* Annual Review of Fluid Mechanics, 1997. **29**: p. 27-64.
62. Carretero Benignos, J.A. and Massachusetts Institute of Technology. Dept. of Mechanical Engineering., *Numerical simulation of a single emitter colloid thruster in pure droplet cone-jet mode*. 2005. p. 117 leaves.
63. Hartman, R.P.A., et al., *The evolution of electrohydrodynamic sprays produced in the cone-jet mode, a physical model.* Journal of Electrostatics, 1999. **47**(3): p. 143-170.
64. Hartman, R.P.A., et al., *Electrohydrodynamic atomization in the cone-jet mode physical modeling of the liquid cone and jet.* Journal of Aerosol Science, 1999. **30**(7): p. 823-849.

65. Yoon, S.S., et al., *Modeling multi-jet mode electrostatic atomization using boundary element methods.* Journal of Electrostatics, 2001. **50**(2): p. 91-108.
66. Zeng, J., D. Sobek, and T. Korsmeyer, *Electro-hydrodynamic modeling of electrospray ionization: Cad for a mu fluidic device - Mass spectrometer interface.* Boston Transducers'03: Digest of Technical Papers, Vols 1 and 2, 2003: p. 1275-1278, 1938.
67. Lastow, O. and W. Balachandran, *Numerical simulation of electrohydrodynamic (EHD) atomization.* Journal of Electrostatics, 2006. **64**(12): p. 850-859.
68. *http://www.flow3d.com*.
69. Valaskovic, G.A., et al., *Attomole-Sensitivity Electrospray Source for Large-Molecule Mass-Spectrometry.* Analytical Chemistry, 1995. **67**(20): p. 3802-3805.
70. Kriger, M.S., K.D. Cook, and R.S. Ramsey, *Durable Gold-Coated Fused-Silica Capillaries for Use in Electrospray Mass-Spectrometry.* Analytical Chemistry, 1995. **67**(2): p. 385-389.
71. Fang, L.L., et al., *Online Time-of-Flight Mass-Spectrometric Analysis of Peptides Separated by Capillary Electrophoresis.* Analytical Chemistry, 1994. **66**(21): p. 3696-3701.
72. Cao, P. and M. Moini, *A novel sheathless interface for capillary electrophoresis/electrospray ionization mass spectrometry using an in-capillary electrode.* Journal of the American Society for Mass Spectrometry, 1997. **8**(5): p. 561-564.
73. Fong, K.W.Y. and T.W.D. Chan, *A novel nonmetallized tip for electrospray mass spectrometry at nanoliter flow rate.* Journal of the American Society for Mass Spectrometry, 1999. **10**(1): p. 72-75.
74. Emmett, M.R. and R.M. Caprioli, *Micro-Electrospray Mass-Spectrometry - Ultra-High-Sensitivity Analysis of Peptides and Proteins.* Journal of the American Society for Mass Spectrometry, 1994. **5**(7): p. 605-613.
75. Gatlin, C.L., et al., *Protein identification at the low femtomole level from silver-stained gels using a new fritless electrospray interface for liquid chromatography microspray and nanospray mass spectrometry.* Analytical Biochemistry, 1998. **263**(1): p. 93-101.
76. Aturki, Z., et al., *On-line CE-MS using pressurized liquid junction nanoflow electrospray interface and surface-coated capillaries.* Electrophoresis, 2006. **27**(23): p. 4666-4673.
77. Edwards, J.L., et al., *Negative mode sheathless capillary electrophoresis electrospray ionization-mass spectrometry for metabolite analysis of prokaryotes.* Journal of Chromatography A, 2006. **1106**(1-2): p. 80-88.
78. *http://www.kiriama.com/kiriama%20single-mode%20polymer%20fibers_009.htm*.
79. Wilm, M.S. and M. Mann, *Electrospray and Taylor-Cone Theory, Doles Beam of Macromolecules at Last.* International Journal of Mass Spectrometry, 1994. **136**(2-3): p. 167-180.

80. Hirt, C.W. and B.D. Nichols, *Volume of Fluid (Vof) Method for the Dynamics of Free Boundaries.* Journal of Computational Physics, 1981. **39**(1): p. 201-225.
81. Melcher, J.R., *Continuum electromechanics*. 1981, Cambridge, Mass.: MIT Press. 1 v. (various pagings).
82. *http://www.flow3d.com/cfd-101/cfd-101-FAVOR.html*.
83. *http://www.flow3d.com/cfd-101/cfd-101-FAVOR-no-loss.html*.
84. Savage, B.M. and M.C. Johnson, *Flow over ogee spillway: Physical and numerical model case study.* Journal of Hydraulic Engineering-Asce, 2001. **127**(8): p. 640-649.
85. *http://www.flow3d.com/cfd-101/cfd-101-free-surface-fluid-flow.html*.
86. Graham T. T. Gibson, R.D.W.a.R.D.O., *Multiple electrosprays generated from a single poly carbonate microstructured fibre.* Mass Spectrometry, 2011.
87. Smith, R.D., et al., *Analytical characterization of the electrospray ion source in the nanoflow regime.* Analytical Chemistry, 2008. **80**(17): p. 6573-6579.
88. Hirt, C.W., *Electro-hydrodynamics of semi-conductive fluids: with application to electro-spraying.* Flow Science Technical Note, 2004. **70**(FSI–04–TN70): p. 1-7.
89. de la Mora, J.F., *The fluid dynamics of Taylor cones.* Annual Review of Fluid Mechanics, 2007. **39**: p. 217-243.
90. Cloupeau, M. and B. Prunetfoch, *Electrostatic Spraying of Liquids in Cone-Jet Mode.* Journal of Electrostatics, 1989. **22**(2): p. 135-159.
91. Hayati, I., A.I. Bailey, and T.F. Tadros, *Investigations into the Mechanisms of Electrohydrodynamic Spraying of Liquids .1. Effect of Electric-Field and the Environment on Pendant Drops and Factors Affecting the Formation of Stable Jets and Atomization.* Journal of Colloid and Interface Science, 1987. **117**(1): p. 205-221.
92. ***FLOW-3D*** *User Manual, Ver. 9.4.*
93. Sen, A.K., J. Darabi, and D.R. Knapp, *Analysis of Droplet Generation in Electrospray Using a Carbon Fiber Based Microfluidic Emitter.* Journal of Fluids Engineering-Transactions of the Asme, 2011. **133**(7).